Microporous and Mesoporous Materials 363 (2024) 112840

Contents lists available at ScienceDirect

Microporous and Mesoporous Materials

journal homepage: www.elsevier.com/locate/micromeso

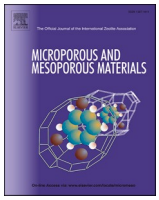

In-depth study of factors affecting the formation of MCM-41-type mesoporous silica nanoparticles

Vicente Candela-Noguera [a,e,**], María Alfonso [a], Pedro Amorós [b], Elena Aznar [a,c,d,e,f], María Dolores Marcos [a,c,d,e,*], Ramón Martínez-Máñez [a,c,d,e,f,***]

[a] Instituto Interuniversitario de Investigación de Reconocimiento Molecular y Desarrollo Tecnológico (IDM), Universitat Politècnica de València, Valencia, Spain
[b] Instituto Universitario de Ciencia de los Materiales (ICMUV), Universitat de València, Catedrático José Beltrán 2, 46980, Paterna, Valencia, Spain
[c] Departamento de Química, Universitat Politècnica de València, Camino de Vera s/n, 46022, Valencia, Spain
[d] CIBER de Bioingeniería, Biomateriales y Nanomedicina, Instituto de Salud Carlos III, Spain
[e] Unidad Mixta UPV-CIPF de Investigación en Mecanismos de Enfermedades y Nanomedicina, Universitat Politècnica de València, Centro de Investigación Príncipe Felipe, Valencia, Spain
[f] Unidad Mixta de Investigación en Nanomedicina y Sensores, Universitat Politècnica de València, IIS La Fe, Valencia, Spain

ARTICLE INFO

Keywords:
Mesoporous silica nanoparticles
MCM-41
Synthesis
Mechanism
Parameters

ABSTRACT

Mesoporous silica nanoparticles (MSN), especially MCM-41 type, have been broadly studied and used in different applications such as catalysis, nanomedicine and environmental science. One of the most advantageous properties of these materials is their easy and tunable synthesis. Nevertheless, in spite of the efforts made by researchers in the last decades, there is still no complete understanding of the mechanism and factors affecting the formation of MCM-41 type MSN, and some parameters are disregarded in the reported synthesis protocols. Considering that the fine-tuning of the parameters affecting nanoparticle synthesis is the basis for obtaining well-defined nanodevices with advanced complex functionalities, an in-depth study of the factors affecting the formation of MCM-41 type MSN is carried out in this work. We analyzed the first stages of MSN formation, namely the silica-surfactant templating and nanoparticle nucleation and growth, and found that hydrolysis and condensation rates play a central role in nanoparticle formation. Furthermore, we found that some disregarded parameters in the MCM-41 type synthesis, such as the stirring strength or the surfactant addition rate, modulate nucleation and growth, influencing the hydrolysis and condensation rates. Finally, we studied the aging and the evolution of the MSN by analyzing the consolidation of the silica framework over time. Therefore, we further elucidate some points about the mechanism and factors affecting the formation of mesoporous silica, which brings us closer to obtaining reproducible, homogeneous and tailored-made MCM-41 type MSN.

1. Introduction

In the last decade, mesoporous silica nanoparticles (MSN) have been widely applied to several fields, including sensing [1], catalysis [2] and biomedicine [3–5] due to their unique properties. Among mesoporous silicas, one of the most commonly studied is the MCM-41 type because of the ordered framework, narrow pore size distribution, cylindrical arrangement of pores, and high specific surface area and volume. In addition, the versatility of MCM-41, in the form of nanoparticles, is demonstrated [6] as their synthesis is easily tunable, producing nanoparticles with different structures, morphologies, sizes, or surface properties [7,8]. These characteristics make MCM-41 type MSN the most extensively studied silica particles in biomedicine [9–11] as sensors [12–15], and in other advanced applications [16–19], compared to other mesostructured silica materials, such as worm-like [20], dendrimer-like [21], or containing disordered pores.

In this context, researchers have pursued the control of particle characteristics, as this allows them to be tailored to the requirements of

* Corresponding author. Departamento de Química, Universitat Politècnica de València, Camino de Vera s/n, 46022, Valencia, Spain.
** Corresponding author. Instituto Interuniversitario de Investigación de Reconocimiento Molecular y Desarrollo Tecnológico (IDM), Universitat Politècnica de València, Valencia, Spain.
*** Corresponding author. Instituto Interuniversitario de Investigación de Reconocimiento Molecular y Desarrollo Tecnológico (IDM), Universitat Politècnica de València, Valencia, Spain.
E-mail addresses: vicanno@etsid.upv.es (V. Candela-Noguera), mmarcos@qim.upv.es (M.D. Marcos), rmaez@qim.upv.es (R. Martínez-Máñez).

https://doi.org/10.1016/j.micromeso.2023.112840
Received 16 May 2023; Received in revised form 14 September 2023; Accepted 30 September 2023
Available online 3 October 2023

the application [8,22]. Therefore, understanding the chemistry involved in the synthesis of MCM-41 type MSN becomes an important goal [23]. Nevertheless, despite the efforts made by some groups, there is still no complete understanding of the parameters affecting the formation of MSN, and some parameters are disregarded in the synthesis protocols.

According to the literature, the formation of MSN could be divided into four steps represented in Fig. 1: silica-surfactant micelles formation (templating), nucleation, growth, and aging [24]. The silica templating is the first step in the MSN formation, for which surfactant molecules are used as scaffold. In the case of MCM-41 type MSN, supramicellar cylinders hexagonally ordered are formed. Different models are proposed to explain the formation of mesoporous silica, such as the liquid crystal templating model [25], the cooperative assembly model [26], the soft-templating model [27], silica polymerization model [28] or swelling-shrinking model [29]. Nevertheless, the most accepted is the cooperative assembly model, which describes that the interaction of the silica moieties with the surfactant molecules is crucial to form the cylindrical micelles, since the surfactant at the concentration used in the synthesis does not reach the critical micellar concentration to form cylindrical micelles by itself [30–32]. Subsequently, the aggregation of silica-surfactant micelles to form initial and small cores provokes the nucleation [33]. These aggregations are possible thanks to shielding the electrostatic repulsion between the hydrolyzed silica species when they bind to the surfactant micelles [34]. These small cores act as nucleation sites, to which the rest of the micelles bind and where a preferential silica polymerization occurs [35,36]. Then, growth means increasing the core size by the aggregation or coalescence with other small cores or simple silica-coated micelles, which align along crystal planes [37]. The growth rate is also associated with the hydrolysis and condensation rate of the silica precursor and can be modified by the presence of co-solvents, amines, or inorganic compounds [34]. Nanoparticles' growth is halted when the charge density reaches a specific value that prevents the deposition of new silicate species [7] or when the materials are consumed [31]. Finally, aging means forming and reorganizing silica bonds, strengthening and consolidating the nanoparticle skeleton. This process is slower than the previous ones. In fact, some studies report that complete silicate condensation takes at least one [7] or one and a half hours [38]. This is why most synthesis protocols leave the mixture of silica precursor and surfactant in the reaction vessel for at least 2 h.

Regarding the synthesis of MSN some parameters have been broadly and deeply analyzed, such as the pH [7,8,23,28,29,31,39–46] and the temperature [7,8,47–52], and they clearly influence MSN formation, modulating the hydrolysis and condensation rates of silica species and affecting to the size of the nanoparticles and their mesostructure. Other parameters, such as the silica precursor used [53–56], the silica/-surfactant ratio [22,57], and the concentration of alcohols added as cosolvents [33,50,58–63] are also commonly studied in the MSN synthesis and their effects on the formation of nanoparticles are clear. However, there are other parameters whose effect on MSN formation remain unclear or are unaccounted for. This is the case of the reaction time [7,38,48,51], which has been studied, but its effect remains controversial [7,22,41,45,50]; the stirring strength, whose effects have been observed [8,47,64–68], but few explanations has been proposed for them; or the silica precursor addition rate.

In the case of MCM-41 type MSN, the synthesis procedure is relatively standardized and based on the conditions employed by Cai et al., in 2001 [37], which remains the most widely used protocol owing to its facile implementation [46]. Yet, this protocol leaves some poorly defined parameters that have been freely interpreted over the last years and whose modifications are not always well studied, such as we mentioned above, the stirring strength or the TEOS addition rate among others.

Taking into account that an understanding of the formation mechanism and parameters affecting the synthesis of nanoparticles is the basis for obtaining well-defined nanodevices that can exhibit advanced complex functionalities, we report herein a study of the MCM-41 type MSNs synthesis to further elucidate some points about the mechanism and factors affecting their formation. For this, we have taken and characterized aliquots during the first stages of MSN formation. In addition, we analyzed the formation of MSN as a function of the volume of TEOS added, the stirring conditions and the TEOS addition rate. Finally, we have also studied the aging processes during the formation of the MSNs. We hope that this study will help researchers to gain a more detailed picture of the various factors that can affect the synthesis of more reproducible and tailored MCM-41-type MSNs.

2. Experimental section

Materials. Tetraethylorthosilicate (TEOS), 1-hexadecyltrimethylammonium bromide (CTAB) and sodium hydroxide (NaOH) were purchased from Sigma-Aldrich. Hydrochloric acid 37% (HCl) was provided by Scharlab.

General techniques. Transmission electron microscopy (TEM), N_2 adsorption-desorption isotherms, powder X-ray diffraction (PXRD), dynamic light scattering (DLS), electrophoretic light scattering (ELS) and solid-state nuclear magnetic resonance (ss-NMR) were used to characterize the prepared materials. The instruments used were the following: JEOL JEM-1010 microscope for TEM images acquisitions; Bruker D8 Advance diffractometer (Cu Kα radiation) for PXRD measurements; Micromeritics ASAP 2010 automated analyzer for the recording of N_2 adsorption-desorption isotherms, samples were degassed at 120 °C in a vacuum overnight. The specific surface areas were calculated from the adsorption data within the low-pressure range using the BET (Brunauer–Emmett–Teller) model. Pore size was determined following the BJH (Barrett–Joyner–Halenda) method. Particle size (DLS) and ʒ potential (ELS) in solution were measured by ZetaSizer Nano ZS (Malvern Instruments Ltd.) equipped with a laser of 633 nm and collecting the signal at 173°. Ss-NMR were performed in Bruker Avance III 400 WB spectrophotometer.

Synthesis of nanoparticles. Different conditions were used to synthesize MCM-41-type nanoparticles, specified in each assay (Results and discussion section). Nevertheless, the assays and synthesis performed during the work were based on a standard synthesis. The standard synthesis was established as follows: 1 g of CTAB (2.74 mmol) was

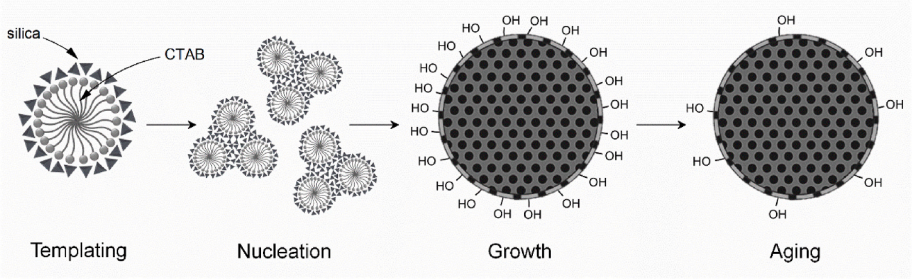

Fig. 1. Schematic representation of the steps involved in the formation of MSN: (a) silica-surfactant micelles formation, (b) nucleation, (c) growth, and (d) aging.

mixed with 480 mL of deionized water in a 1L (10.5 cm of outer diameter) cylindrical beaker. The mixture was heated at 50 °C to dissolve the surfactant and stirred with a cylindrical and plain magnetic stir bar (60 mm long and 15 mm diameter) at 500 rpm. Then, 280 mg of NaOH (7 mmol) dissolved in 3.5 mL of deionized water were added to reach a pH of 12.16, and the temperature solution was adjusted to 80 °C. A watch glass was placed to cover the beaker to minimize solvent evaporation and prevent the volume from decreasing during the reaction. When the temperature reached 80 °C, 5 mL of TEOS (25.7 mmol) were added dropwise (5 mL min^{-1}) using a syringe and needle. Soon after, a white precipitate appeared. The mixture was stirred for 2 h. After this time, the suspension was cooled at room temperature (measured pH 11.75). The solid product was then vacuum filtered with a Buchner over a filter paper (Whatman™ Grade 3 MM Chr), and deionized water was added until the suspension reached neutral pH. Then, the solid was dried under vacuum and ground to obtain a white powder. After the synthesis, nanoparticles were calcined at 550 °C using an oxidant atmosphere for 5 h to remove the surfactant. Calcination was only performed in the last aging study, since the previous samples were taken as aliquots to be characterized with TEM and DLS.

Image analysis. Transmission electron microscopy was performed to acquire a comprehensive representation of each sample to check the size and shape of synthesized nanoparticles. At least 100 particles for each sample were counted to obtain a representative size distribution of the particles. In the case of non-spherical nanoparticles, the size was measured in the longer direction.

DLS measurements. DLS measurements on aliquots samples were performed directly on the corresponding aliquots samples or by diluting them with distilled water. The rest of the DLS samples were resuspended and generously sonicated in distilled water (1 mg NP mL^{-1}). After that, they were briefly spun in a centrifuge (a spin pulse to 8600 rcf) to remove the presence of large aggregates or sedimentation, which could disturb the DLS measurements. The average of three measurements was calculated and represented. ELS samples were prepared by suspending, then generously sonicating the nanoparticles in distilled water (10 mg NP mL^{-1}) and then spinning briefly (a centrifuge pulse to 8600 rcf) to remove the presence of large aggregates or sedimentation, which could disturb the electrophoretic movement measurements of the particles.

3. Results and discussion

3.1. Templating, nucleation and growth studies

To analyze the initial stages of the formation of the MCM41-type MSN, some aliquots were taken while TEOS was being added, as "snapshots". Beside, a quenching of the reaction was carried out after the aliquots were taken to avoid further reaction in the tubes. The aliquots were named as "quenched aliquots", QA. Aliquots were taken just after adding 1, 2, 3, 4 and 5 mL of TEOS in a standard synthesis (see Experimental Section) procedure (then, taken at 12, 24, 36, 48 and 60 s), and the samples obtained were named **QA1**, **QA2**, **QA3**, **QA4** and **QA5**, respectively. Besides, an aliquot called **A0** was taken before starting the TEOS addition to analyze the pre-existence of CTAB micelles. The quenching was performed by diluting 5 times the aliquots with deionized water and placing them in an ice bath.

DLS measurements and representative TEM images can be seen in Fig. 2 (and Fig. S1 and Fig. S2, Supplementary Information). In the case of the **A0** sample, DLS reveals a peak of ca. 5.5 nm, attributed to CTAB micelles, which are confirmed in TEM images, despite the low electron density of organic matter. TEM images show worm-like aggregates of

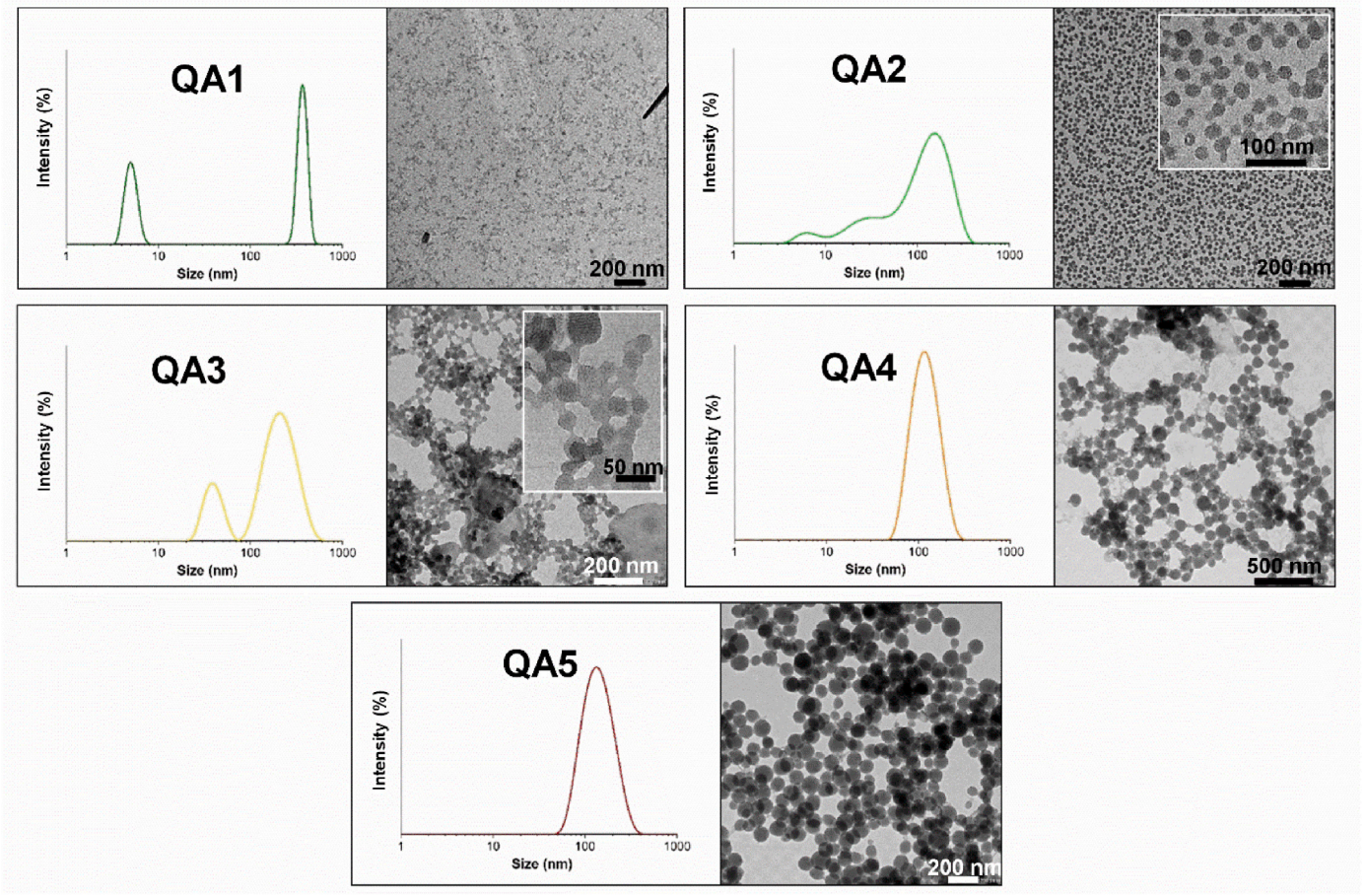

Fig. 2. Size distribution according to Intensity PSD analysis and TEM images of **QA1**, **QA2**, **QA3**, **QA4** and **QA5**.

small dots of about 5–6 nm (Fig. S1, Supplementary Information). These images are similar to previously reported TEM observations of CTAB solutions [69–71]. For **QA1**, two DLS peaks are observed at 5 nm and 370 nm. It is suggested that the former corresponds to CTAB micelles (or single silica-surfactant complexes) and the latter is suggested to correspond to large entities such as CTAB crystallizations or aggregates of amorphous silica, which are also observed in the TEM images. For **QA2**, DLS shows a population at ca. 6 nm (presumably corresponding to CTAB micelles), and peaks at 32 nm and 155 nm. In the TEM images, small nanoparticles still in formation can be seen, sized at ca. 28–30 nm. In addition, some larger particles are observable in additional TEM images of QA2 (Fig. S2, Supplementary Information), whose sizes vary from 30 to 300 nm, which correspond to the larger population in DLS. DLS curve of **QA3** displays two evident populations at 38 nm and 205 nm. TEM images show a first population corresponding to small mesoporous nanoparticles in formation, and a second one formed by particles in the range from 150 to 400 nm. **QA4** and **QA5** display single populations at 114 nm and 132 nm in DLS analysis, respectively. TEM images showed for **QA4** and **QA5** populations of nanoparticles already formed of ca. 88 ± 8 nm and 98 ± 12 nm, accordingly.

The results show that the nanoparticles are forming and growing progressively, from the 6 nm CTAB micelles, then seeds of 30 and 40 nm approximately, to finally fully formed nanoparticles of ca. 90–100 nm. Some bigger size minority populations are formed and can be observed in DLS and TEM in some samples, such as **QA2** (DLS population at 155 nm) and **QA3** (DLS population at 205 nm) (see sample **QA2** and **QA3** in Fig. S2, Supplementary Information). It has to be remarked that Intensity PSD analysis overestimates the larger populations in DLS curves.

All these observations suggest that templating, nucleation and growth processes are very quick, with fully formed nanoparticles being observed even before 5 min of reaction. Besides, in the first aliquots (**QA1** and **QA2**), we can find CTAB micelles and silica-surfactant complexes of ca. 6 nm (in DLS curves), which are consumed as the reaction progresses, since they are not measurable in the following aliquots. Additionally, applying higher magnification in the **QA** TEM images (Fig. S2, Supplementary Information), the typical 2D hexagonal arrangement of pores were shown as both hexagonal pores or parallel cylindrical channels (in **QA3**, **QA4** and **QA5**). Even in the case of **QA2**, when the particles are only small seeds, a quasi-hexagonal arrangement of pores was observed. These observations demonstrate that the hexagonal arrangement and templating of silica already occur at the initial stages of the process, in contrast to the observations made by Sadasivan et al. [27], who described the formation of disordered silica-surfactant micelles when small nanoparticles (seeds) are formed. Therefore, as TEOS is added, the nanoparticles grow from seeds via the deposition of new surfactant-silica micelles, which increase the number of cylindrical micelles arranged hexagonally and elongate them.

3.2. The role of TEOS amount in nucleation and growth of MSN

The study of quenched aliquots (QA) above allowed us to follow the progress of the formation of the particles throughout the synthesis procedure, however, two simultaneous parameters were modified: the amount of TEOS added, and the reaction time. In order to establish the individual role of the TEOS availably in the formation of the nanoparticles, we decided to study the samples obtained when different amounts of TEOS are added to the reaction but, in this case, allowing the mixture to proceed until the end of the standard reaction procedure (2

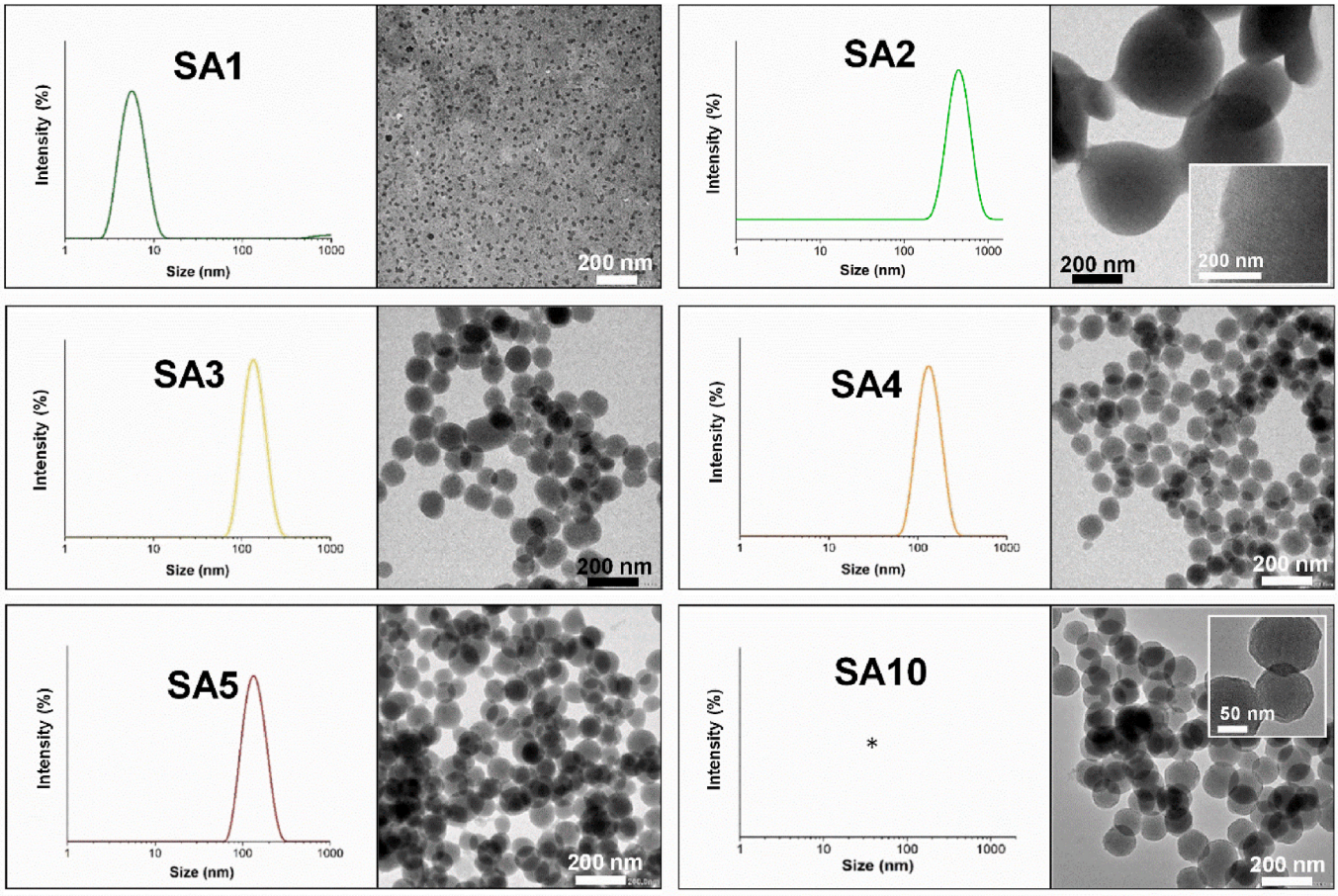

Fig. 3. Size distribution according to Intensity PSD analysis and TEM images of **SA1**, **SA2**, **SA3**, **SA4**, **SA5**, and **SA10**. * DLS measurements of **SA10** cannot performed due to the great presence of agglomerates in the sample.

h). Therefore, we synthesized nanoparticles following the standard conditions, but adding 1, 2, 3, 4, 5 (standard volume) and 10 mL of TEOS. After stirring for 2 h, aliquots were taken and characterized. The aliquots were named **SA1**, **SA2**, **SA3**, **SA4, SA5,** and **SA10** ("stirred aliquots", SA), respectively.

The aliquots were analyzed by DLS and TEM (Fig. 3 and Fig. S3, Supporting Information). DLS and TEM images of **SA1** are similar to those of **QA1** (*vide ante*). This fits with previous results in which 1 mL of TEOS is not enough to produce nanoparticles but only small silica-surfactant complexes. Regarding **SA2**, **SA3**, **SA4** and **SA5**, clear, single, and narrow populations can be observed on DLS curve, centered at 458, 135, 132, and 134 nm, respectively. **SA10** cannot be measured properly in DLS due to the great amounts of agglomerates in the sample. TEM pictures show that **SA2** material consists of sub-micron mesoporous particles of ca. 401 ± 99 nm. In the case of **SA3**, **SA4** and **SA5**, TEM images show standard MCM41-type MSN, being somewhat larger in the case of **SA3**. What regards to **SA10**, TEM pictures show MCM41-type MSN with a layer of amorphous silica in the nanoparticles' surface, whose thickness is 6.8 ± 2.2 nm (Fig. S4, Supplementary Information). The sizes of the nanoparticles from TEM are 110 ± 22 nm in **SA3**, 94 ± 12 nm in **SA4**, 95 ± 14 nm in **SA5**, and 119 ± 18 nm in **SA10**.

The most striking fact of this assay is the significant increase in the size of the particles in sample **SA2**. We can also observe an increase, but to a lesser extent, in **SA3** compared to the other samples (**SA4** and **SA5**). While 1 mL of TEOS (**SA1**) is not enough to nucleate and form MSN, when 2 mL of TEOS were added (**SA2**), the nucleation and growth processes are boosted, and large nanoparticles are formed. Other authors have also observed this phenomenon [72], but no explanations were given. It is reported that tuning pH, temperature or solvent provoke noticeable changes in nanoparticles' size, giving the influence that these factors have on the hydrolysis and condensation rates and the silica solubility. However, in our case the studied samples (SA) are synthesized in the same conditions in terms of pH, temperature and solvent. Therefore, we hypothesize that the larger size of nanoparticles in **SA2** and, to a lesser extent in **SA3**, can be explained considering both the LaMer-based growth mechanism [73,74] and the influence of the TEOS amount on the hydrolysis and condensation rates. According to LaMer-based growth mechanism and our observations, the formation of nanoparticles can be divided into three phases (Fig. 4). The first phase corresponds to the lag time [74], in which hydrolysis of silica precursor is predominant, and therefore the concentration of silica monomers per time increases in parallel to the hydrolysis rate. The condensation is negligible, so no nucleation or growth takes place. This is because, on the one hand, the self-nucleation threshold is not reached and, on the other hand, there are not nucleation sites over which silica monomers can deposit and polymerize. In this phase, silica monomers form spherical surfactant-silica micelles (sized at ca. 5–6 nm) and correspond with **QA1**. The second phase starts when the self-nucleation threshold is achieved, which implies i) the condensation of silica monomers to form oligomers, ii) the silica oligomers cooperate with surfactant to form cylindrical micelles, iii) several spherical and cylindrical micelles nucleate to form seeds, and iv) the consumption of silicate monomers until falling below the self-nucleation threshold. This phase corresponds with **QA2** and partially **QA3**. Then, starts the third phase, the silica condensation is predominant and it preferentially deposit into already existing nuclei, which promotes the growth of formed seeds into nanoparticles (corresponding to **QA4** and **QA5**). The growth is stopped when the concentration of silicate monomers decreases until the critical supersaturation level, below which they remain dissolved in equilibrium as monomers.

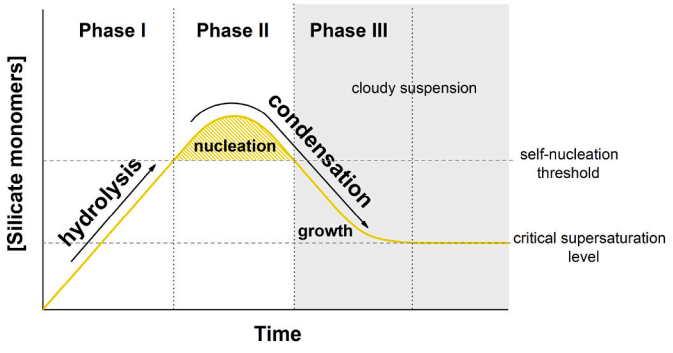

Fig. 4. A) LaMer-based growth model proposed for MCM41-type MSN. Dotted lines divide the three phases. Dashed lines indicate the self-nucleation threshold and the critical supersaturation level. Gray area means the phase in which the suspensions appears cloudy.

On the other hand, it can be claimed that the lower amount of TEOS in MSN synthesis (in **SA2** and **SA3**) limits and slows down the reaction progress, that is, the number of TEOS molecules hydrolyzed and silicate monomers polymerized per time. Considering both phenomena (LaMer-based growth and TEOS amount limitation), we can hypothesize that, when smaller amounts of TEOS are added (e.g. 2 or 3 mL), the proportion of silicate monomers above this self-nucleation threshold is lower. This means that the number of nucleation seeds formed are lower, and this gives, in turn, larger particles, since the silicate monomers available after the nucleation are driven to grow the existent seeds but not to form new ones. In contrast, according to our observations, when higher concentrations of TEOS are added (**SA10**), the nanoparticles formed are not smaller, but larger. Thus, we hypothesize that the hydrolysis and condensation progress practically at maximum rates, that is, the ratio of silica monomers formation per time reaches its maximum value. Therefore, the proportion of silicate monomers above the self-nucleation threshold does not increase, leading to a higher growth, instead a higher nucleation. Furthermore, the surface layer of amorphous silica formed in **SA10** suggests the consumption of surfactant micelles that act as template.

To reinforce these results, we decided to determine the time it takes for the reaction mixture to turn turbid white once different amounts of TEOS are added. The emergence of a white suspension have been reported by several authors in the range of ca. 1–10 min [7,34,60,72,75–79]. The cloudy appearance is described to correspond with the seeds' growth and formation of nanoparticles that reach a certain size threshold [80,81], which some authors set at 25 nm [82]. Then, this time can be correlated with the end of nucleation step and the beginning of growth step. The volumes tested in this case were 1, 1.5, 1.75, 2, 3, 4, 5, 7.5, and 10 mL of TEOS. Considering previous observations, we decided to instantly add the precursor (instead of 5 mL min^{-1}) to eliminate the TEOS addition rate as a variable and limiting factor. The results show that the time required to obtain a white suspension increases as the amount of TEOS decreases (Fig. 5). This increasing is especially steep when the amount of TEOS is lower than 2 mL, although the time interval in which the transition from translucent to cloudy appearance occurs is broad and less clear. In contrast, when at least 2 mL of TEOS are added this interval is narrower. On the other hand, it should also be noted that 1 mL of TEOS was not enough to give a cloudy suspension. Finally, it is also observable that, at the studied conditions, the time it takes the reaction to turn cloudy reaches it minimum value from 7.5 mL (t = 31 s).

These results reinforce the hypothesis of LaMer-based growth and the influence of the TEOS amount in the hydrolysis and condensation progression. Therefore, the behavior of the reaction when different amounts of TEOS are added can be explained, considering the TEM images and the time it takes the reaction to turn cloudy (Fig. 6). As Fig. 6 indicates, when lower amounts of TEOS are added, the slope in which the silicate monomers appear is shallower, the time required to reach the growth step are higher, and then, the cloudy appearance emerges later. In contrast, above 5 mL the time required is very similar (t = 36 s in the case of adding 5 mL of TEOS and t = 31 s in the case of 7.5 and 10 mL), which suggest that the slope barely increases. Therefore, it can be claimed that the hydrolysis and condensation rates reach their

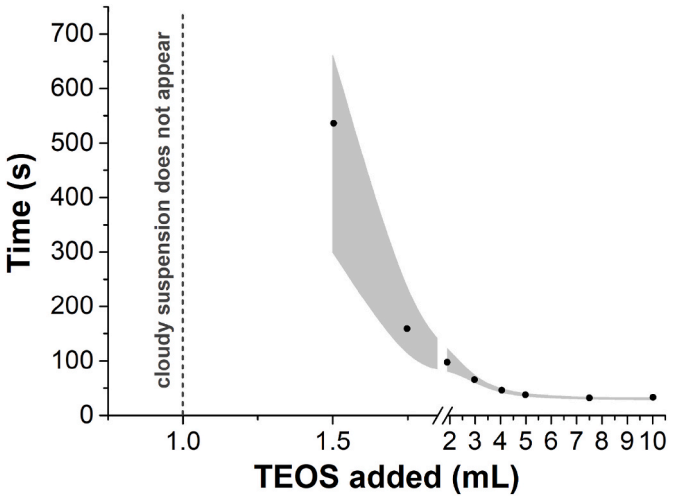

Fig. 5. Representation of the time required for the reaction mixture to become cloudy, measured as a function of the amount of TEOS added. Gray area means the time interval in which the transition from translucent to cloudy appearance occurs.

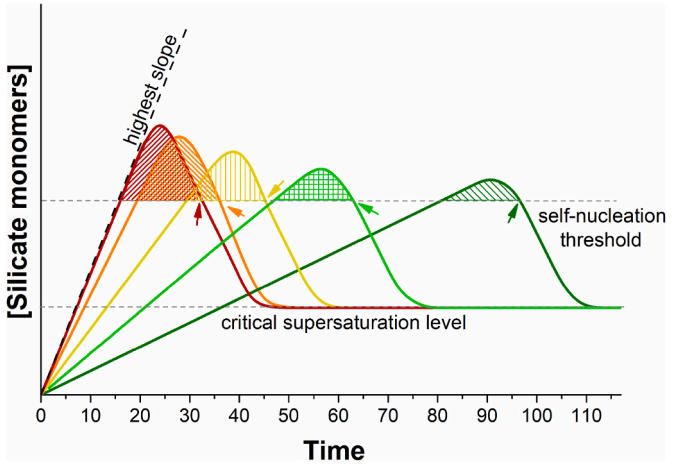

Fig. 6. LaMer-based growth mechanism proposed for explaining the results obtained when 2 mL (dark green), 3 mL (light green), 4 mL (yellow), 5 mL (orange) and 10 mL (red) of TEOS are added instantly. Arrows indicate the time in which the formed seeds start to grow.

maximum values at least from 7.5 mL of TEOS addition.

3.3. *Influence of stirring strength on MSN formation*

As we mentioned and it is widely described, the MSN formation is mainly conducted by hydrolysis and condensation rates. These reactions are principally modulated by the pH, the temperature, and the solvent. These parameters are fairly studied. However, there are other disregarded parameters whose influence on the hydrolysis and condensation rates are less studied. One of these parameters is the stirring rate. The stirring rate has been reported to modulate the size of nanoparticles. At low stirring speed, large-sized nanoparticles are formed [47,64]. Meanwhile, the increase in stirring speed leads to the formation of smaller nanoparticles [47,65–68]. In addition, strong stirring rates provoke morphological regularity deterioration due to shearing forces originated [8]. However, these studies are sometimes incomplete and no explanation has been given to establish a correlation between the stirring strength and the nanoparticles size in the case of MSN.

To improve our knowledge about this phenomenon, different samples were prepared by modifying the stirring rate (350 rpm, 500 rpm, 900 rpm and 1200 rpm). The samples named **MSN-350 rpm**, **MSN-500 rpm** (corresponding to the standard synthesis), **MSN-900 rpm** and **MSN-1200 rpm** were characterized by TEM and DLS. According to TEM pictures (Fig. 7), the diameter of the nanoparticles decreases with increasing stirring rates until reaching a minimum value of around 80 nm when using 900 rpm (**MSN-350 rpm** averaged at 112 nm, **MSN-500 rpm** at 89 nm, both **MSN-900 rpm** and **MSN-1200 rpm** at 80 nm). In addition, it is also observable that the morphology of the nanoparticles becomes more irregular when the stirring speed increases. Thus, **MSN-350 rpm** and **MSN-500 rpm** tend to have a smooth surface and a spherical shape, but **MSN-900 rpm** and especially **MSN-1200 rpm** are poorly formed and their surface is rough. TEM images also indicate that higher stirring rate leads to a higher number of fusions between nanoparticles. The tendency observed in DLS curves (Fig. S5, see Supplementary Information) is in line with that found in TEM images, except for **MSN-1200 rpm** in which a slightly increase in the diameter is observed (i.e. **MSN-350 rpm** centered at 175 nm, **MSN-500 rpm** at 162 nm, **MSN-900 rpm** at 147 nm and **MSN-1200 rpm** at 168 nm).

In addition, the time taken from the reaction to become cloudy was also measured, this time by tuning the stirring speed. On this occasion, the amount of TEOS added was 3 mL (at 5 mL min^{-1}), considering that, in standard conditions, the white turbidity was reached when 4 mL of TEOS were added and this could mask the effect of tuning the stirring rate. For these assays, the stirring was adjusted to 350, 500, 900, and 1200 rpm. It can be observed that the time required to appear the white turbidity decreases as the stirring rate increases when 3 mL of TEOS are added (from 95 s at 350 rpm to 26 s at 1200 rpm) (Fig. 8).

Considering the previous results, it can be stated that the effect of stirring speed on the size and morphology of MSN is through the influence on the rate of hydrolysis and condensation rate, since the time taken for the reaction to become cloudy is also affected. We can suggest that at higher stirring speeds, the oil drops of TEOS formed after being added to the aqueous solution are split due to the high radial flow and the shearing forces derived. This provokes the surface of the interface between TEOS oil drops and aqueous solution to increase, as it has been previously described [29], and thus, more TEOS can be hydrolyzed, since hydrolysis occurs in this interface [68]. The promotion of hydrolysis rate increases the slope in which silicate monomers appear per time, and then, their number above the nucleation threshold. As we suggested before, this explains the formation of higher amounts of seeds and, in turn, smaller nanoparticles. In contrast, when lower stirring rates are applied, the interface surface between oil and aqueous phase is lower, which leads to a decrease in the hydrolysis rate, the formation of less seeds and larger nanoparticles. A similar correlation between stirring rate and nanoparticles size was reported by Yokoi et al. for non-porous silica nanospheres [68]. Moreover, the increase in fusions between nanoparticles (observed by TEM and also suggested by DLS measurements) and the deformation of their shape (observed by TEM) with increasing stirring speed (especially in **MSN-900 rpm** and **MSN-1200 rpm**) could be the consequence of turbulence and chaotic behavior. Under these conditions the collisions between cores are more common, the fluid dynamics becomes inhomogeneous and phenomena such as swirling and cavitation appear. In this line, it has been described that cavitation can disturb even the mesoporous geometry and order [64]. In addition, high stirring speeds can lead to less controllable hydrolysis and condensation steps, increasing fusions and uneven nanoparticle growth.

Since the radial flow depends not only on the stirring speed but also on the shape of the magnetic stirrer, we have also studied in detail the later effect. A sample called **MSN-egg** was synthesized using an egg-shaped stir bar at 500 rpm (see set up in Fig. S6, Supplementary Information). The nanoparticles obtained were compared with those obtained with the **MSN-500 rpm** conditions synthesized using a cylindrical-shaped stir bar. We observed that the stirring force achieved with the egg-shaped magnetic stirrer is lower than with the cylindrical-

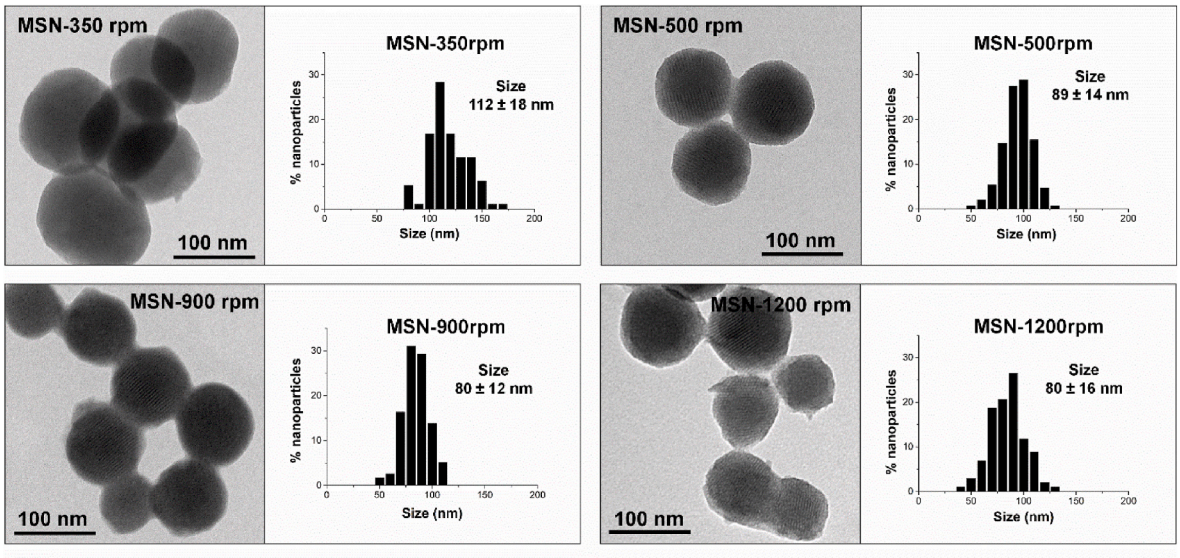

Fig. 7. Representative TEM images of **MSN-350 rpm**, **MSN-500 rpm**, **MSN-900 rpm**, and **MSN-1200 rpm**. In addition, histograms with particle size distribution of the samples are also shown.

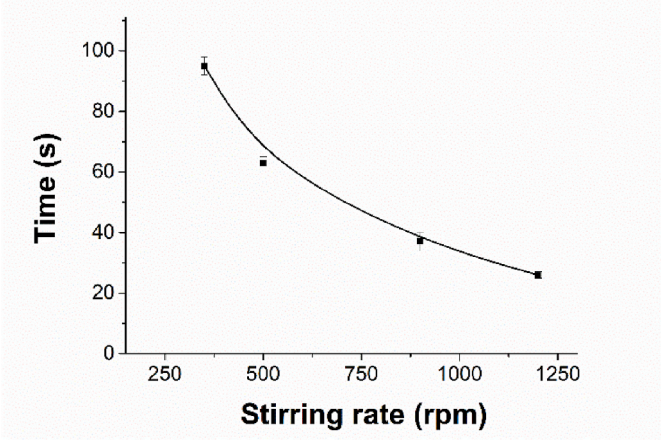

Fig. 8. Representation of the time required for the reaction mixture to become cloudy, measured as a function of the stirring rate.

shaped one. Therefore, as expected, the samples stirred with an egg-shaped magnetic stirrer (**MSN-egg**) are larger than the ones stirred with the cylindrical-shaped stirrer at the same speed (**MSN-500 rpm**) and rather similar to those obtained at a lower speed (**MSN-350 rpm**) when using a cylindrical stirrer. The average diameter of the nanoparticles measured for **MSN-egg** using TEM images is 112 ± 19 nm, and their hydrodynamic diameter by DLS is centered at 183 nm (Fig. S6, Supplementary Information).

In summary, it can be pointed out that the stirring strength affects the MSN formation in different manners. On the one hand, it can vary the size of the nanoparticles, due to the lower or higher homogenization of the reaction mixture, which modulates the amount of TEOS available to be hydrolyzed and, in turn, the nucleation and growth process. On the other hand, it can drive to different regularity of their morphology and surface, and promote the fusion and coalescence between nanoparticles. This can be produced due to the turbulence, chaotic behavior, cavitation, and swirling phenomena, when the reaction mixture is stirred vigorously. Thus, the control of the stirring during the MCM41-type MSN synthesis is crucial for controlling the characteristics of the nanoparticles [74]. Furthermore, it is important to control not only the stirring speed, but also the magnetic stir bar's size and shape, as they also influence in the formation of the nanoparticles. At this point, it is essential to note that stir bar characteristics or stirring details are not usually reported in the literature despite their proven importance. This issue must be especially cared for industry production, in which the set up and scale up are not trivial matters.

3.4. TEOS addition rate effect

Preparation recipes to obtain MCM-41 nanoparticles normally describe the TEOS addition rate as "drop by drop", "dropwise" or similar. Moreover, there are some works that reported a specific rate, such as 0.1 [50], 0.25 [83], 0.38 [40,84], 0.5 [45], 1 [46,47,64,85], or 1.45 mL min^{-1} [48]. However, most of these works did not explain the criteria to establish this choice. Some authors, such as Chiang et al., considered the addition rate of TEOS to have a neglected effect on the morphology and structure of MSN [45]. On the contrary, Moongraksathum et al. defended that the rate of TEOS addition, along with the stirring speed and concentration of surfactant, influences the characteristics of MSN [86]. Oliveira et al. [87] reported a synthesis in which TEOS was added in two steps and tested the second addition in controlled dropwise or not controlled. The authors observed differences between both conditions, such as the formation of a bimodal distribution in particle size, variations in relative surface area and differences concerning the aggregation of nanoparticles. In another study, Lechevallier et al. [83] obtained a quite polydispersed sample when TEOS was added at 0.25 mL min^{-1}. He et al. [84] added TEOS at 0.38 mL min^{-1}, and the nanoparticles were highly fused and the relative surface area was low (ca. 860 m^2 g^{-1}) compared to standard MCM-41 type MSN.

Aiming to improve the understanding of the implications of the TEOS addition rate, we have synthesized MSN adding 5 mL of TEOS at 0.25 mL min^{-1}, 1 mL min^{-1}, 5 mL min^{-1} and instantly. The samples were named **MSN-0.25**, **MSN-1**, **MSN-5,** and **MSN-instant**, respectively.

The different samples obtained were characterized by DLS and TEM. TEM images of the synthesized samples are shown in Fig. 9. **MSN-0.25** displays a very broad size distribution for the MSN. Specifically, three differentiable populations of MSN are observed: i) spherical nanoparticles in the 70–120 nm range; ii) rod-like nanoparticles with the long axis ranging from 140 nm to 250 nm and the short axis from 90 nm to 130 nm; and iii) bean-like nanoparticles, which were a kind of bent rods, whose diameters are from 250 nm to more than 400 nm. **MSN-1** shows two different populations: i) spherical nanoparticles from 70 to 120 nm, analogues to the spherical ones in **MSN-0.25**, and ii) rod-like

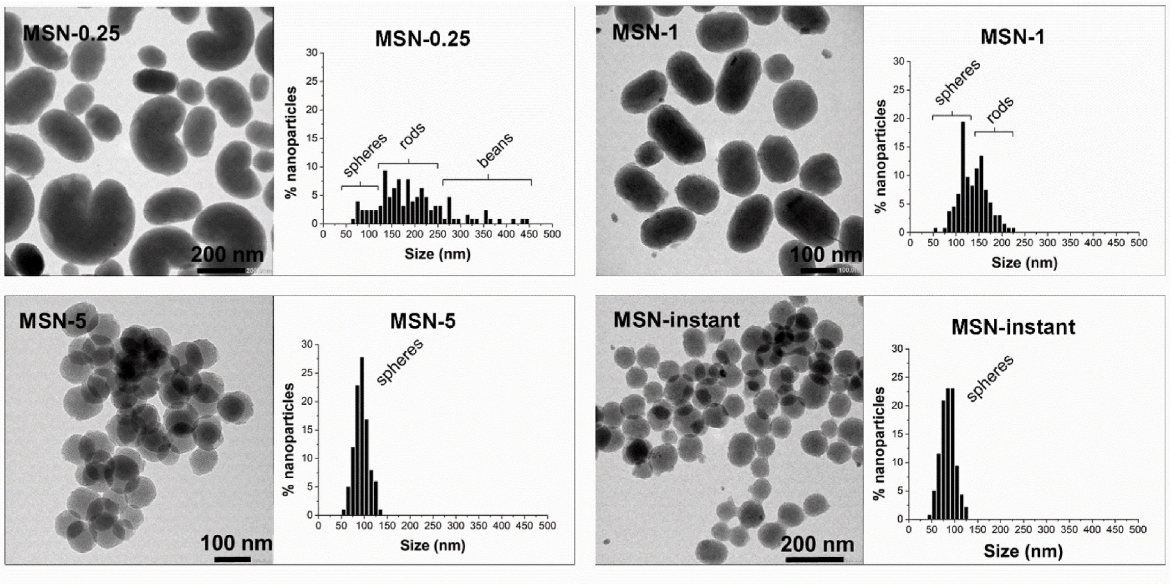

Fig. 9. TEM images of **MSN-0.25**, **MSN-1**, **MSN-5**, and **MSN-instant**. In addition, histograms with particle size distribution (from TEM images) and MSN morphology indications are showed.

nanoparticles, whose long axis ranges from 140 to 230 nm (a bit smaller than rods found on **MSN-0.25**), and short axis in the 90–120 nm range. In the case of **MSN-5** and **MSN-instant**, only one population of spherical nanoparticles was found, in the range from 60 nm to 130 nm (centered at 94 ± 15 nm), and 50 nm–120 nm (centered at 85 ± 16 nm), respectively. Besides, nanoparticles from **MSN-5** have a more regular and smoother surface than the ones in **MSM-instant**, for which some roughness can be seen. All the populations present in TEM images visible mesoporosity. Considering fusions between nanoparticles, **MSN-0.25** and **MSN-1** materials show few visible linkages, whereas **MSM-instant** clearly shows bridges between nanoparticles and coalescing nanoparticles. DLS curves of the samples are displayed in Fig. S7, Supporting Information.

The time it takes the reaction to become cloudy was also measured. 5 mL of TEOS were added at 0.25 mL min^{-1}, 0.5 mL min^{-1}, 1 mL min^{-1}, 5 mL min^{-1} and instantly. The results are reported in Fig. 10. It is observed that the slower the addition rates, the longer it takes to observe white turbidity (from 36 s for instantaneous addition to ca. 600 s when adding TEOS at 0.25 mL min^{-1}).

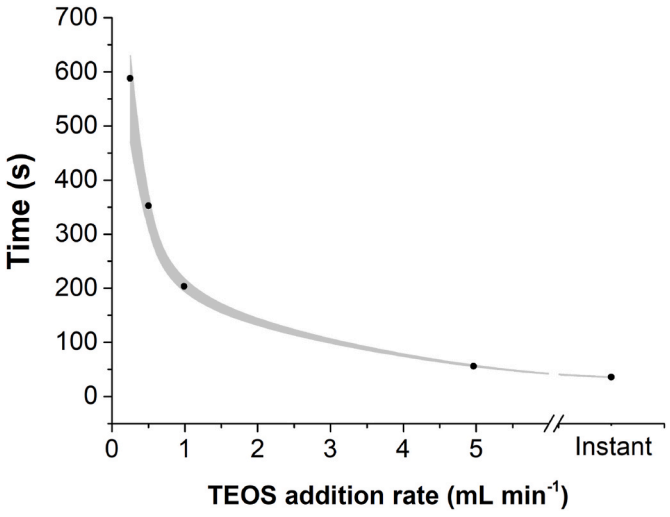

Fig. 10. Representation of the time required for the reaction mixture to become cloudy, measured as a function of the TEOS addition rate. Gray area means the time interval in which the transition from translucent to cloudy appearance occurs.

The results indicate that the rate of TEOS addition also influences the rate of hydrolysis and condensation, as well as the nucleation and growth of nanoparticles, by means of restricting the availability of TEOS at a given time. It is observed that the lower the amount of TEOS available, the slower the formation of nanoparticles, following the same explanation that found at different volume of TEOS added or stirring speeds (*vide ante*). This is especially observable when low addition rates are used, such as in **MSN-0.25**, in which the three populations observed correspond to three different growth phases. These results can also be explained according to the LaMer-based growth mechanism, considering the progression of three differentiated nucleation cycles (Fig. 11). This can be described as follows. Firstly, spherical nanoparticles are formed from an initial seed formation, in which reaction turn cloudy (at ca. 630 s). Secondly, when spheres are formed, and the silica continues depositing over them, the nanoparticles grow mainly in the axis parallel to the channels, forming rod-like nanoparticles. These can be defined as extended spheres, in which the smaller axis is similar to the diameter of the spheres, and the long axis coincides with the direction of the CTAB templated channels. In parallel, remaining surfactant-silica complexes aggregate as TEOS is added and a second nucleation step starts, forming additional spherical nanoparticles. Thirdly, as the reaction goes by, rod-like nanoparticles from the previous step can still accumulate more silica and grow. When they reach approximately 250 nm on the long axis, their structure begins to bend and bean-shaped nanoparticles appear. The spherical nanoparticles formed at second nucleation seed formation can also suffer additional growth and acquire rod morphology. In this latter stage, a third additional formation of seeds occurs, because new silica precursor molecules are added to the suspension until the 1200 s. Thus, new spherical nanoparticles are formed.

Regarding **MSN-1**, the process can be seen as similar to that observed in **MSN-0.25**, but the third step does not occur. In this case, the addition rate was faster and therefore the availability of TEOS was higher from the beginning. At initial stages, a greater amount of nucleation seeds is formed; hence, the added silica precursor is not enough to form bean-shaped nanoparticles. In other words, since most of the TEOS has already been used to grow the higher number of nuclei, a new nucleation cycle does not occur, as the nucleation threshold is not reached. **MSN-5** and **MSN-instant** only produce the spherical population as the addition rate of silica precursor is fast enough to form a sufficient number of

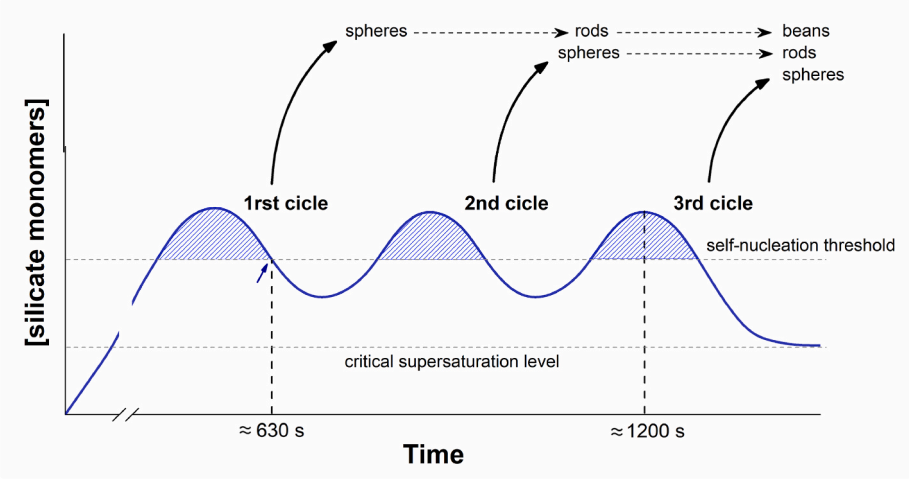

Fig. 11. LaMer-based growth mechanism proposed for explaining the sequential nucleation in the case of **MSN-0.25**. Arrow indicates the estimated time when it takes the reaction to turn cloudy.

nucleation seeds to use all the silica available. Since no additional TEOS is added once the nanoparticles are formed, the hydrolyzed silica species are distributed homogeneously among the nuclei to form monodisperse nanoparticles.

Bean-shaped nanoparticles formation was also reported by Beltrán-Osuna et al. [64] when they applied a very low stirring speed and a TEOS addition rate of 1 mL min^{-1}. To further check the influence of low stirring speed in the formation of bean-shaped nanoparticles, we synthesized and characterized a sample at standard conditions (TEOS added at 5 mL min^{-1}), but stirred at 250 rpm (**MSN-250 rpm**). TEM images of **MSN-250 rpm** (Fig. S8, Supplementary Information) also show the presence of three populations found in **MSN-0.25**: spherical, rod-shaped, and bean-shaped nanoparticles. DLS curve is also similar to **MSN-0.25** (Fig. S8, Supplementary Information).

Therefore, both stirring rate and TEOS addition rate influence the amount of TEOS available to be hydrolyzed and then the number of nuclei formed. The formation of a few nuclei in the initial stages leads to the formation of large nanoparticles. However, the progressive emergence of new silica precursor monomers from hydrolyzed TEOS, both due to the slow addition rate of TEOS or the low stirring speed, can lead to new nucleation cycles and a multimodal population of nanoparticles.

3.5. Aging and reaction time

The first steps in the synthesis of the nanoparticles (surfactant-silica micelles formation, nucleation and growth) occur in less than 10 min, as

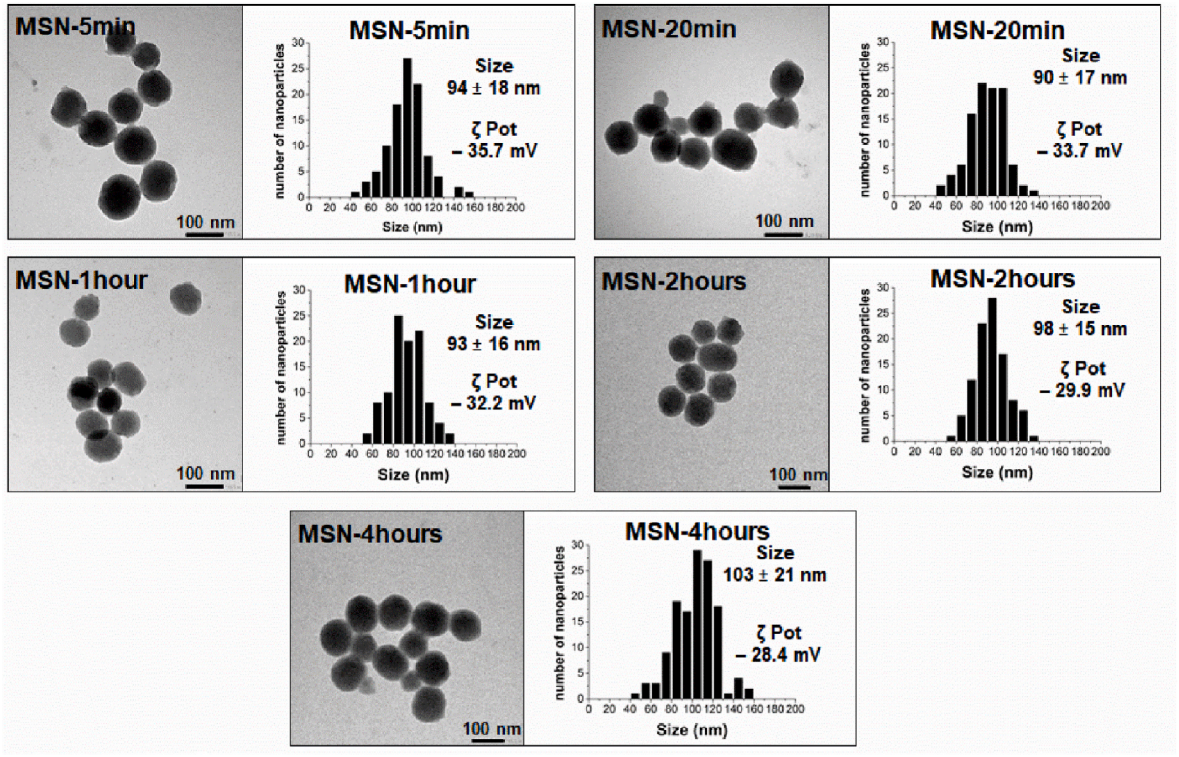

Fig. 12. Size distribution according to Intensity PSD analysis, ζ potential value and TEM images of **MSN-5min**, **MSN-20min**, **MSN-1hour**, **MSN-2hours** and **MSN-4hours**. In addition, histograms with particle size distribution (from TEM images) and ζ potential values.

we have demonstrated in the previous sections and other authors also described [29,88]. This means that the additional time left for the reaction corresponds to an aging process. To study this more in detail, we have characterized several samples after the complete addition of TEOS (5 mL) following a standard synthesis, at different reaction times (5 min, 20 min, 1 h, 2 h and 4 h), which were named **MSN-5min**, **MSN-20min**, **MSN-1hour**, **MSN-2hours** and **MSN-4hours**, respectively. TEM images, DLS and ELS, Si^{29}-ssNMR, PXRD and nitrogen adsorption-desorption studies were performed to characterize the nanoparticles. This study is similar to the one performed by Catalano et al. [7], who characterized samples at 7 min, 30 min, 1 h, 1.5 h and 2 h. Nevertheless, we obtained different conclusions compared with these authors, as mentioned throughout this section.

TEM pictures (Fig. 12) of calcined samples, show completely formed nanoparticles. However, the samples obtained after shorter reaction times (**MSN-5min** and **MSN-20min**) show nanoparticles with an irregular surface. Nanoparticles range from ca. 90–100 nm in TEM images as histograms of distribution size show (Fig. 12). DLS measurements of calcined samples were also performed (Fig. S9, Supplementary Information). **MSN-5min** shows two populations at 185 and 702 nm, **MSN-20min** one broad population at 148 nm, and **MSN-1hour**, **MSN-2hours** and **MSN-4hours** narrow distributions at 159 nm, 158 nm and 174 nm, respectively. TEM images and DLS measurements show that the size distribution becomes narrower from 5 min to 2 h but increasing their breadth at 4 h. ELS measurements of calcined samples show a lower negative ζ Potential over time (Fig. 12), from −35.7 mV for **MSN-5min** to −28.4 mV for **MSN-4hours**.

From these data, it could be affirmed that 5 min of aging are enough to obtain samples similar to common MSN in size and morphology. In fact, the evolution of nanoparticles from 5 min to 2 h (the standard reaction time) barely supposes an increase in the size of the nanoparticles. These results disagree with Catalano et al. [7] studies, which suggest an increase from 108 nm after 7 min to 159 nm after 2 h. We observe in TEM and DLS results that the aging step after the growth of the nanoparticles is necessary to reorganize and level the size between nanoparticles. This can be done by a mass transfer to larger nanoparticles which grow at the expense of the dissolution of smaller nanoparticles; a phenomenon known as Ostwald ripening [89].

Additionally, the measurement of ζ potential allows for monitoring the progression of the reaction. Since the negative charge of calcined MSN comes from silanolate groups, the decrease of ζ potential means the progressive condensation of these groups. Therefore, the degree of condensation of the nanoparticles is expected to be higher in those samples in which the reaction time is longer and vice versa. These observations agree with some authors [7,38] that reported that some hours are required to complete the condensation process. Still, they are also in conflict with the results of Catalano et al. [7], which did not find a correlation between the reaction evolution and the ζ potential value. This can be explained by the differences in the synthesis process as Catalano et al. washed the nanoparticles with ethanol and extracted the surfactant by refluxing with ethanol-HCl.

We also studied as-made and calcined nanoparticles by powder X-ray

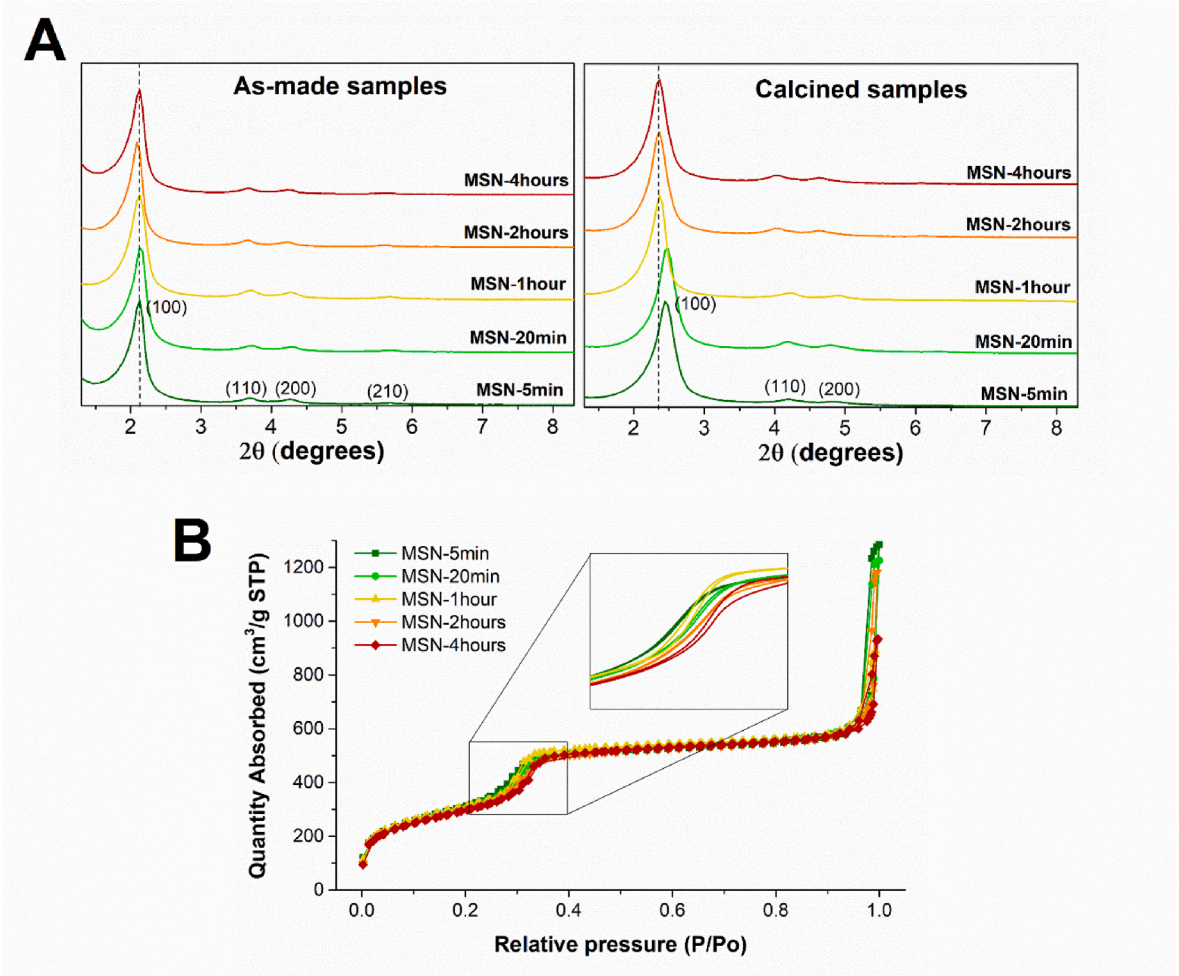

Fig. 13. A) PRXD patterns of as-made and calcined samples. Dashed lines indicate the position of peak (100) in the cases of **MSN-4hours** as-made and calcined. B) N_2 adsorption-desorption isotherms of calcined samples (**MSN-5min**, **MSN-20min**, **MSN-1hour**, **MSN-2hours**, and **MSN-4hours**). Inset: magnification of capillary condensation region.

diffraction techniques (PXRD), and the results are shown in Fig. 13A and summarized in Table 1. Diffractograms of the as-made materials are similar in all the samples (from **MSN-5min** to **MSN-4hours**) in terms of both the position and the broadness of their peaks. Therefore, this fact suggests that the supra-micellar hexagonal structure is formed already after 5 min with the same characteristics as the standard synthesis ((100), (110), (200) and (210) reflections are present). The rapid formation of the hexagonal structure is already reported by other authors [88]. The main peak, corresponding to the (100) reflection in these samples, falls in the narrow range of 2.09–2.14°, corresponding to a unit cell ca. 4.76–4.88 nm. Furthermore, the full width at half maximum (FWHM) calculated for this peak ranges from 0.22 to 0.24. In the case of the calcined nanoparticles, the peaks corresponding to the reflections (100), (110), and (200) are still observable, but (210) does not, due to the partial loss of long-range ordering typical after calcination. In this context, there is greater variability in the position and width of the peaks compared with the as-made samples. Moreover, the peak (100) is found progressively at a lower diffraction angle with the progression of the reaction (from 2.45 in **MSN-5min** to 2.36 in **MSN-4hours**). On the other hand, the broadness of the peak (100) (FWHM) is greater in the samples with a lower reaction time (0.32 and 0.30 for **MSN-5min** and **MSN-20min**, respectively) and smaller when the reaction time increases (0.28, 0.26 and 0.28 for **MSN-1hour**, **MSN-2hours** and **MSN-4hours**, accordingly). Comparing as-made and calcined samples, the unit cell contraction appears to be lower as the reaction synthesis progresses and vice versa. Thus, in **MSN-5min** and **MSN-20min,** the unit cell shrinks 0.65 and 0.68 nm, respectively, while in **MSN-1hour**, **MSN-2hours** and **MSN-4hours** the unit cell contracts 0.52, 0.49 and 0.49, correspondingly. Besides, the ratio between the FWHM of the (100) peak after and before calcination behaves in the same vein, being higher in **MSN-5min** and **MSN-20min** samples (1.45 and 1.30) and smaller in **MSN-1hour**, **MSN-2hours** and **MSN-4hours** ones (1.17, 1.18 and 1.27).

As we observed in previous results, the PXRD diffractograms show that the porous hexagonal arrangement is formed from the first minutes of reaction. This is maintained along the reaction time in both as-made and calcined samples. Once again, these results dissent from the study of Catalano et al. [7] as they observed unresolved peaks in as-made early samples due to a disruption in the structure, which ethanol washing and surfactant extraction processes may provoke.

Moreover, our samples show the typical shift of the diffractogram peaks to higher 2θ values (reduction in d-spacing) and the loss of long-range ordering in calcined samples, which is related to the unit cell contraction or shrinkage provoked by the calcination process. Our results suggest that cell contraction and structure disruption are inversely correlated with reaction time and aging. In this sense, when weak structures such as **MSN-5min** and **MSN-20min** are calcined, they tend to suffer more significant contraction and disorder of the mesostructure [57,65], which is reflected in larger peaks shifts (unit cell contraction) and broadening of the peak (100) (FWHM ratio). By contrast, the samples **MSN-1hour**, **MSN-2hours** and **MSN-4hours** are more consolidated and suffer less shrinkage and structure disruption.

Measurements of isothermal adsorption-desorption of nitrogen were also performed to characterize the pore size, pore volume, and surface area (Fig. 13B and Table 2). The isotherms obtained are similar in all the samples studied. They all exhibit a type IV isotherm typical of mesoporous materials. The main difference observed is that the sharp jump at intermediate partial pressures, corresponding to the capillary condensation region, shifts to higher pressures as the synthesis time increases (from 0.28 p/p_o in **MSN-5min** to 0.32 p/p_o in **MSN-4hours**). This tendency can be seen in Table 2, in which the pore size increases progressively with the reaction time (from 2.65 nm in **MSN-5min** to 2.88 nm in **MSN-4hours**). In the case of specific surface area, a decrease was observed oppositely to the reaction time (from 1157 $m^2\ g^{-1}$ in **MSN-5min** to 1082 $m^2\ g^{-1}$ in **MSN-4hours**). Regarding the pore volume, no clear tendency is observed, and it seems to be constant in the different samples (in the range from 0.97 to 1.01 $cm^3\ g^{-1}$). In addition, considering the PXRD and N_2 isotherms results, we have calculated the wall thickness for the different materials by subtracting the pore size value from the unit cell value, but no clear tendency was observed as a function of the reaction time.

The results observed in N_2 adsorption-desorption isotherms fit with the expected tendency in accordance with PXRD data. Then, the consolidation of the structure over reaction time reduces the shrinkage of the mesostructure. As a consequence of that, we find that the pore size is larger as the synthesis time increases. Additionally, the decrease in specific surface area in the samples with longer aging can also be an indication of the consolidation of their structure, which suffers fewer defects and nooks in the surface, in contrast to those samples stirred only for 5 or 20 min. On the other hand, the minor variations in the wall thickness calculated for the different materials suggests the reaction time is not affecting this parameter. The changes in the unit cell measured in the PXRD analysis correspond with the decrease in pore size, which is observed in the N_2 adsorption measurements.

To reliably verify the degree of condensation, the samples **MSN-5min**, **MSN-1hour**, **MSN-2hours** and **MSN-4hours** were analyzed by Si^{29}-ss-NMR (Fig. 14). The NMR spectra of the samples (Fig. 14C) show 3 peaks at ca. 90, 100 and 110 ppm, corresponding to $(HO)_2Si\text{-}(OSi)_2$ (Q^2),

Table 2
Mesoporosity of samples as a function of their reaction time.

sample	BET surface ($m^2\ g^{-1}$)	BJH pore volume ($cm^3\ g^{-1}$)	BJH pore size (nm)	wall thickness (nm)
MSN-5min	1157	0.97	2.65	1.51
MSN-20min	1131	0.98	2.73	1.40
MSN-1hour	1134	1.01	2.71	1.53
MSN-2hours	1101	0.98	2.84	1.55
MSN-4hours	1082	0.98	2.88	1.44

Table 1
PXRD measurements of samples as a function of their synthesis time.

	As made			Calcined			Compared data		
Sample	Peak [100] (2θ)	Unit cell (nm)	FWHM peak [100]	Peak [100] (2θ)	Unit cell (nm)	FWHM peak [100]	Peak [100] shift (2θ)	Unit cell contraction (nm)	FWHM ratio
MSN-5min	2.12	4.81	0.22	2.45	4.16	0.32	0.33	0.65	1.45
MSN-20min	2.12	4.81	0.23	2.47	4.13	0.30	0.38	0.68	1.30
MSN-1hour	2.14	4.76	0.24	2.41	4.24	0.28	0.27	0.52	1.17
MSN-2hours	2.09	4.88	0.22	2.32	4.39	0.26	0.23	0.49	1.18
MSN-4hours	2.12	4.81	0.22	2.36	4.32	0.28	0.24	0.49	1.27

A

$$DK = \frac{4 \cdot Q^4 + 3 \cdot Q^3 + 2 \cdot Q^2 + 1 \cdot Q^1}{400}$$

B

	Relative content of silica species (%)			DC
	Q^2	Q^3	Q^4	
MSN-5min	32.8	41.7	25.5	73.2
MSN-1hour	17.1	47.4	35.6	79.6
MSN-2hours	10.2	48.6	41.2	82.8
MSN-4hours	4.6	74.0	21.4	79.2

C

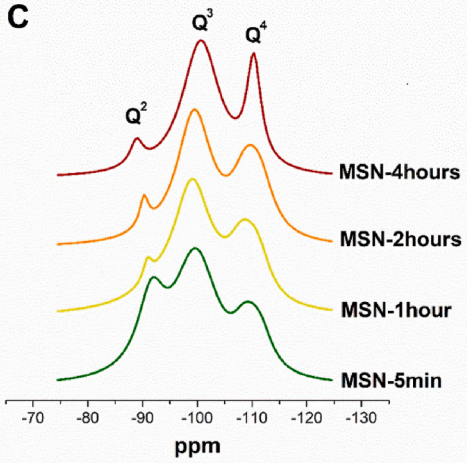

Fig. 14. Si^{29}-ss-NMR characterization of samples. A) Degree of condensation (DC) equation, B) Table with relative content of silica species, and C) Si^{29}-ss-NMR spectra of as-made samples (**MSN-5min**, **MSN-1hour**, **MSN-2hours**, and **MSN-4hours**).

$(HO)Si\text{-}(OSi)_3$ (Q^3) and $Si(OSi)_4$ (Q^4) silicon species. The area under the curve (AUC) was calculated for each peak by deconvolution of the spectra, fitting them in a Gaussian distribution. At first glance, the spectra show a progressive decrease in the Q^2 signal and an increase in Q^3 and Q^4. Regarding the AUC calculated from spectra deconvolution and Gaussian fitting, it is observed a decreasing tendency in the AUC of Q^2 with the progression of the reaction time ($32.8 > 17.1 > 10.2 > 4.6$) with a concomitant increase of the AUC of Q^3 ($41.7 < 47.4 < 48.6 < 74.0$) and Q^4, except for **MSN-4hours** ($25.5 < 35.6 < 41.2 > 21.4$). The degree of condensation (DC) was also calculated, according to the equation reported by Barczak (Fig. 14A) [90]. The variation of the DC parameter reflects that the connectivity of silica in the lattice increases progressively with the reaction time, except for **MSN-4hours** ($73.2 < 79.6 < 82.8 > 79.2$). The lower condensation degree observed in the case of **MSN-4hours** can be explained by some hypothesis. On the one hand, it must be considered that the hydrolysis and condensation of silanol groups are both continuous reactions during the synthesis. Therefore, it can be hypothesized that in the interval from 2 h to 4 h, regarding the silica species equilibrium, the hydrolysis can surpass the condensation, decreasing the condensation rate. Considering the changes in hydrolysis/condensation tendency, similar behavior can be observed in Ref. [45], in which nanoparticles grow from 2 to 4 h, but become smaller from 4 to 10 h. On the other hand, the reduction of condensation degree can be explained due to the mild growth in the nanoparticles from 2 h to 4 h. In this context, the silica deposited to grow the nanoparticles can be less condensed than the nanoparticle already formed at 2 h, reducing the global condensation degree of the nanoparticles. Finally, it can be also hypothesized that the narrow shape of Q^4 peak in **MSN-4hours** provokes that, after the deconvolution, a portion of Q^4 peak is wrongly integrated as Q^3 peak, and therefore, the AUC of Q^4 peak decreases. However, qualitatively the Q^4 peak height can indicate an increase in Q^4 connections in comparison to **MSN-2hours**, in which the peak height is much lower.

These results confirm that once the nanoparticles are formed, the silica condensation inside the material is a slow process that can take several hours. This agrees with previous reports in which a partial condensation was reported for a solid obtained after 3 min of stirring [24] that after aging resulted in a more stable and well-ordered MCM-41 structure [48,51] due to a gradual increase in the degree of condensation, which confers the nanoparticles greater resistance to the shrinkage caused by calcination [65].

4. Conclusions

We have systematically studied the factors affecting the formation of MCM41-type MSN. On the one hand, we have studied and characterized the initial stages of MSN formation, especially concerning the nucleation and growth processes. Therefore, we have demonstrated that the formation of MSN is not only affected by the pH, the temperature or the solvent, as it has been widely studied, but also by the amount of TEOS added, the stirring rate and the TEOS addition rate. We have observed that these parameters influence the silica available to be hydrolyzed and then, affect the hydrolysis and condensation rates, which play a central role in the development of MSN. Our observations can be explained by the LaMer-based growth model, by which nucleation or growth are predominant depending on the self-nucleation threshold. We have also described the phenomenon of sequential nucleation cycles that occurs in the reaction and produces heterogeneous samples when the TEOS is slowly available to be hydrolyzed.

On the other hand, we have analyzed the evolution and aging of MSN. We have observed the rapid formation of MCM41-type MSN, suggesting that the templating, nucleation and growth steps occur in less than 5 min. Then, the evolution and aging of MSN after 5 min mainly evolves towards the increase of the condensation inside the nanoparticles and their strengthening. Also, aging implies that silica is redistributed between nanoparticles (Ostwald ripening).

In the literature, we can find very complex and smart nanodevices developed from MSN, including MCM-41 type ones, with a wide range of functionalities, and they have been applied to many fields. They have been functionalized with alkoxysilanes, molecular gates, dyes and biomolecules; loaded with drugs, medical image contrasts, dyes and nucleic acids, doped with metallic and semimetallic ions, organometallic compounds, etc. Nevertheless, the detailed information about the synthesis conditions of MSN is scorned in most of the reported works. However, as we demonstrate herein, small changes in the synthesis process can have a high impact in the final material obtained. Through our study, a more profound knowledge about the synthesis mechanism of MCM-41-type MSN has been obtained, especially concerning the parameters that can modulate the hydrolysis and condensation rate, as well as the nucleation and growth processes. This understanding could provide a solid basis to improve the control of the synthesis of nanoparticles and obtain a more reproducible and controlled MCM-41-type MSN.

CRediT authorship contribution statement

Vicente Candela-Noguera: Writing – original draft, Investigation,

Data curation, Conceptualization. **María Alfonso:** Investigation. **Pedro Amorós:** Investigation, Data curation. **Elena Aznar:** Supervision, Investigation. **María Dolores Marcos:** Writing – review & editing, Supervision, Investigation, Funding acquisition, Data curation. **Ramón Martínez-Máñez:** Writing – review & editing, Supervision, Investigation, Funding acquisition.

Declaration of competing interest

The authors declare that they have no known competing financial interests or personal relationships that could have appeared to influence the work reported in this paper.

Data availability

Data will be made available on request.

Acknowledgment

Vicente Candela-Noguera thanks the Spanish Government for his fellowship (FPU15/02753). This research was supported by projects PID2021-126304OB-C41, PID2021-126304OB-C43 and PID2021-128141OB-C22 funded by MCIN/AEI/10.13039/501100011033/ and by European Regional Development Fund - A way of doing Europe. This study also forms part of the Advanced Materials programme (MFA/2022/049 and MFA/2022/053) and was supported by MCIN with funding from European Union NextGenerationEU (PRTR-C17.I1) and by Generalitat Valenciana. This study was also supported by Generalitat Valenciana (CIPROM/2021/007). The authors also thank the Electron Microscopy Service at UPV for support.

Appendix A. Supplementary data

Supplementary data to this article can be found online at https://doi.org/10.1016/j.micromeso.2023.112840.

References

[1] F. Sancenón, L. Pascual, M. Oroval, E. Aznar, R. Martínez-Máñez, Gated silica mesoporous materials in sensing applications, ChemistryOpen 4 (2015) 418–437, https://doi.org/10.1002/open.201500053.
[2] C.M.A. Parlett, K. Wilson, A.F. Lee, Hierarchical porous materials: catalytic applications, Chem. Soc. Rev. 42 (2013) 3876–3893, https://doi.org/10.1039/c2cs35378d.
[3] A. García-Fernández, E. Aznar, R. Martínez-Máñez, F. Sancenón, New advances in in vivo applications of gated mesoporous silica as drug delivery nanocarriers, Small 16 (2020), 1902242, https://doi.org/10.1002/smll.201902242.
[4] M. Manzano, M. Vallet-regí, Mesoporous silica nanoparticles in nanomedicine applications, J. Mater. Sci. Mater. Med. 29 (2018) 65, https://doi.org/10.1007/s10856-018-6069-x.
[5] I.I. Slowing, J.L. Vivero-Escoto, C.W. Wu, V.S.Y. Lin, Mesoporous silica nanoparticles as controlled release drug delivery and gene transfection carriers, Adv. Drug Deliv. Rev. 60 (2008) 1278–1288, https://doi.org/10.1016/j.addr.2008.03.012.
[6] E. Garrido, et al., A sensitive nanosensor for the in situ detection of the cannibal drug, ACS Sens. 5 (2020) 2966–2972, https://doi.org/10.1021/acssensors.0c01553.
[7] F. Catalano, P.P. Pompa, Design rules for mesoporous silica toward the nanosize: a systematic study, ACS Appl. Mater. Interfaces 11 (2019) 47237–47246, https://doi.org/10.1021/acsami.9b16135.
[8] Y. Chen, et al., The complete control for the nanosize of spherical MCM-41, J. Nanosci. Nanotechnol. 12 (2012) 7239–7249, https://doi.org/10.1166/jnn.2012.6459.
[9] A. Llopis-Lorente, B. Lozano-Torres, A. Bernardos, R. Martínez-Máñez, F. Sancenón, Mesoporous silica materials for controlled delivery based on enzymes, J. Mater. Chem. B 5 (2017) 3069–3083, https://doi.org/10.1039/C7TB00348J.
[10] M. Vallet-Regí, F. Schüth, D. Lozano, M. Colilla, M. Manzano, Engineering mesoporous silica nanoparticles for drug delivery: where are we after two decades? Chem. Soc. Rev. 51 (2022) 5365–5451, https://doi.org/10.1039/D1CS00659B.
[11] F. Tang, L. Li, D. Chen, Mesoporous silica nanoparticles: synthesis, biocompatibility and drug delivery, Adv. Mater. 24 (2012) 1504–1534, https://doi.org/10.1002/adma.201104763.
[12] E. Garrido, E. Climent, M.D. Marcos, F. Sancenón, K. Rurack, R. Martínez-Máñez, Dualplex lateral flow assay for simultaneous scopolamine and “cannibal drug” detection based on receptor-gated mesoporous nanoparticles, Nanoscale 14 (2022) 13505–13513, https://doi.org/10.1039/D2NR03325A.
[13] F. Sancenõn, L. Pascual, M. Oroval, E. Aznar, R. Martínez-Máñez, Gated silica mesoporous materials in sensing applications, ChemistryOpen 4 (2015) 418–437.
[14] E. Climent, M. Biyikal, D. Gröninger, M.G. Weller, R. Martínez-Máñez, K. Rurack, Multiplexed detection of analytes on single test strips with antibody-gated indicator-releasing mesoporous nanoparticles, Angew. Chem. Int. Ed. 59 (2020) 23862–23869, https://doi.org/10.1002/anie.202009000.
[15] E. Garrido, et al., A sensitive nanosensor for the in situ detection of the cannibal drug, ACS Sens. 5 (2020) 2966–2972, https://doi.org/10.1021/acssensors.0c01553.
[16] A. Estepa-Fernández, et al., Engineering nanoparticle communication in living systems by stigmergy: an application to enhance antitumor therapy in triple-negative breast cancer, Nano Today 48 (2023), 101692, https://doi.org/10.1016/j.nantod.2022.101692.
[17] B. de Luis, et al., Nanoprogrammed cross-kingdom communication between living microorganisms, Nano Lett. 22 (2022) 1836–1844, https://doi.org/10.1021/acs.nanolett.1c02435.
[18] B. de Luis, A. Llopis-Lorente, F. Sancenón, R. Martínez-Máñez, Engineering chemical communication between micro/nanosystems, Chem. Soc. Rev. 50 (2021) 8829–8856, https://doi.org/10.1039/D0CS01048K.
[19] B. de Luis, et al., A chemical circular communication network at the nanoscale, Chem. Sci. 12 (2021) 1551–1559, https://doi.org/10.1039/D0SC04743K.
[20] K. Zhang, et al., Facile large-scale synthesis of monodisperse mesoporous silica nanospheres with tunable pore structure, J. Am. Chem. Soc. 135 (2013) 2427–2430, https://doi.org/10.1021/ja3116873.
[21] S. Malekmohammadi, et al., Nonordered dendritic mesoporous silica nanoparticles as promising platforms for advanced methods of diagnosis and therapies, Mater. Today Chem. 26 (2022), 101144, https://doi.org/10.1016/j.mtchem.2022.101144.
[22] G. Lelong, S. Bhattacharyya, S. Kline, T. Cacciaguerra, M.A. Gonzalez, M.-L. L. Saboungi, Effect of surfactant concentration on the morphology and texture of MCM-41 materials, J. Phys. Chem. 112 (2008) 10674–10680, https://doi.org/10.1021/jp800898n.
[23] S.H. Wu, H.P. Lin, Synthesis of mesoporous silica nanoparticles, Chem. Soc. Rev. 42 (2013) 3862–3875, https://doi.org/10.1039/c3cs35405a.
[24] L. Jin, S.M. Auerbach, P.A. Monson, Simulating the formation of surfactant-templated mesoporous silica materials: a model with both surfactant self-assembly and silica polymerization, Langmuir 29 (2013) 766–780, https://doi.org/10.1021/la304475j.
[25] J.S. Beck, et al., A new family of mesoporous molecular sieves prepared with liquid crystal templates, J. Am. Chem. Soc. 114 (1992) 10834–10843, https://doi.org/10.1021/ja00053a020.
[26] A. Monnier, et al., Cooperative formation of inorganic-organic interfaces in the synthesis of silicate mesostructures, Science 261 (1993) 1299–1303, https://doi.org/10.1126/science.261.5126.1299.
[27] S. Sadasivan, C.E. Fowler, D. Khushalani, S. Mann, Nucleation of MCM-41 nanoparticles by internal reorganization of disordered and nematic-like silica - surfactant clusters, Angew. Chemie - Int. Ed vol. 41 (2002) 2151–2153, https://doi.org/10.1002/1521-3773(20020617)41:12<2151::AID-ANIE2151>3.0.CO;2-U.
[28] J. Frasch, B. Lebeau, M. Soulard, J. Patarin, R. Zana, In situ investigations on cetyltrimethylammonium surfactant/silicate systems, precursors of organized mesoporous MCM-41-type siliceous materials, Langmuir 16 (2000) 9049–9057, https://doi.org/10.1021/la000295u.
[29] Z. Yi, et al., A new insight into growth mechanism and kinetics of mesoporous silica nanoparticles by in situ small angle X-ray scattering, Langmuir 31 (2015) 8478–8487, https://doi.org/10.1021/acs.langmuir.5b01637.
[30] K.J. Edler, Current understanding of formation mechanisms in surfactant-templated materials, Aust. J. Chem. 58 (2005) 627–643, https://doi.org/10.1071/CH05141.
[31] F. Lu, S.H. Wu, Y. Hung, C.Y. Mou, Size effect on cell uptake in well-suspended, uniform mesoporous silica nanoparticles, Small 5 (2009) 1408–1413, https://doi.org/10.1002/smll.200900005.
[32] S.C. Chien, et al., Molecular simulations of the synthesis of periodic mesoporous silica phases at high surfactant concentrations, J. Phys. Chem. C 121 (2017) 4564–4575, https://doi.org/10.1021/acs.jpcc.6b09429.
[33] J. Gu, W. Fan, A. Shimojima, T. Okubo, Organic–inorganic mesoporous nanocarriers integrated with biogenic ligands, Small 3 (2007) 1740–1744, https://doi.org/10.1002/smll.200700311.
[34] R. Narayan, U.Y. Nayak, A.M. Raichur, S. Garg, Mesoporous silica nanoparticles: a comprehensive review on synthesis and recent advances, Pharmaceutics 10 (2018) 1–49, https://doi.org/10.3390/pharmaceutics10030118.
[35] R.I. Nooney, D. Thirunavukkarasu, Y. Chen, R. Josephs, A.E. Ostafin, Synthesis of nanoscale mesoporous silica spheres with controlled particle size, Nature 14 (2002) 4721–4728, https://doi.org/10.1021/cm0204371.
[36] J. Schmitt, et al., Outset of the morphology of nanostructured silica particles during nucleation followed by ultrasmall-angle X-ray scattering, Langmuir 32 (2016) 5162–5172, https://doi.org/10.1021/acs.langmuir.6b00572.
[37] Q. Cai, Z.S. Luo, W.Q. Pang, Y.W. Fan, X.H. Chen, F.Z. Cui, Dilute solution routes to various controllable morphologies of MCM-41 silica with a basic medium, Chem. Mater. 13 (2001) 258–263, https://doi.org/10.1021/cm990661z.
[38] J. Zhang, Z. Luz, D. Goldfarb, EPR studies of the formation mechanism of the mesoporous materials MCM-41 and MCM-50, J. Phys. Chem. B 101 (1997) 7087–7094, https://doi.org/10.1021/jp9709621.

[39] C.J. Brinker, Hydrolysis and condensation of silicates: effects on structure, J. Non-Cryst. Solids 100 (1988) 31–50, https://doi.org/10.1016/0022-3093(88)90005-1.
[40] Z.A. Qiao, L. Zhang, M. Guo, Y. Liu, Q. Huo, Synthesis of mesoporous silica nanoparticles via controlled hydrolysis and condensation of silicon alkoxide, Chem. Mater. 21 (2009) 3823–3829, https://doi.org/10.1021/cm901335k.
[41] E. Yamamoto, K. Kuroda, Colloidal mesoporous silica nanoparticles, Bull. Chem. Soc. Jpn. 89 (2016) 501–539, https://doi.org/10.1246/bcsj.20150420.
[42] E. Yamamoto, K. Kuroda, Preparation and controllability of mesoporous silica nanoparticles, in: Enzymes, Elsevier Inc., 2018, pp. 1–10, https://doi.org/10.1016/bs.enz.2018.09.001.
[43] F. Rizzi, et al., High surface area mesoporous silica nanoparticles with tunable size in the sub-micrometer regime: insights on the size and porosity control mechanisms, Molecules 26 (2021) 4247, https://doi.org/10.3390/molecules26144247.
[44] J. Rathousky, M. Zukalova, P.J. Kooyman, A. Zukal, Synthesis and characterization of colloidal MCM-41, Colloids Surfaces A Physicochem. Eng. Asp. 241 (2004) 81–86, https://doi.org/10.1016/j.colsurfa.2004.04.014.
[45] Y.D. Chiang, H.Y. Lian, S.Y. Leo, S.G. Wang, Y. Yamauchi, K.C.W. Wu, Controlling particle size and structural properties of mesoporous silica nanoparticles using the taguchi method, J. Phys. Chem. C 115 (2011) 13158–13165, https://doi.org/10.1021/jp201017e.
[46] M. Varache, I. Bezverkhyy, L. Saviot, F. Bouyer, F. Baras, F. Bouyer, Optimization of MCM-41 type silica nanoparticles for biological applications: control of size and absence of aggregation and cell cytotoxicity, J. Non-Cryst. Solids 408 (2015) 87–97, https://doi.org/10.1016/j.jnoncrysol.2014.10.020.
[47] X. Lv, L. Zhang, F. Xing, H. Lin, Controlled synthesis of monodispersed mesoporous silica nanoparticles: particle size tuning and formation mechanism investigation, Microporous Mesoporous Mater. 225 (2016) 238–244, https://doi.org/10.1016/j.micromeso.2015.12.024.
[48] M. Yu, et al., A simple approach to prepare monodisperse mesoporous silica nanospheres with adjustable sizes, J. Colloid Interface Sci. 376 (2012) 67–75, https://doi.org/10.1016/j.jcis.2012.03.014.
[49] N.A. Zainal, S.R.A. Shukor, H.A.A. Wab, K.A. Razak, Study on the effect of synthesis parameters of silica nanoparticles entrapped with rifampicin, Chem. Eng. Trans. 32 (2013) 2245–2250, https://doi.org/10.3303/CET1332375.
[50] P. Khodaee, N. Najmoddin, S. Shahrad, The effect of ethanol and temperature on the structural properties of mesoporous silica synthesized by the sol-gel method, J. Tissues Mater. 1 (2018) 10–17, https://doi.org/10.22034/JTM.2018.67254.
[51] L. Li, J. Song, J. Wang, W. Fan, Controllable synthesis of mesoporous silica with hierarchical architecture, Mater. Express 7 (2017) 283–290, https://doi.org/10.1166/mex.2017.1381.
[52] S. Ma, Y. Wang, Y. Zhu, A simple room temperature synthesis of mesoporous silica nanoparticles for drug storage and pressure pulsed delivery, J. Porous Mater. 18 (2011) 233–239, https://doi.org/10.1007/s10934-010-9375-3.
[53] T.N.M. Bernards, M.J. van Bommel, A.H. Boonstra, Hydrolysis-condensation processes of the tetra-alkoxysilanes TPOS, TEOS and TMOS in some alcoholic solvents, J. Non-Cryst. Solids 134 (1991) 1–13, https://doi.org/10.1016/0022-3093(91)90005-Q.
[54] H. Yamada, C. Urata, E. Yamamoto, S. Higashitamori, Y. Yamauchi, K. Kuroda, Effective use of alkoxysilanes with different hydrolysis rates for particle size control of aqueous colloidal mesostructured and mesoporous silica nanoparticles by the seed-growth method, ChemNanoMat 1 (2015) 194–202, https://doi.org/10.1002/cnma.201500010.
[55] M.J. Hollamby, D. Borisova, P. Brown, J. Eastoe, I. Grillo, D. Shchukin, Growth of mesoporous silica nanoparticles monitored by time-resolved small-angle neutron scattering, Langmuir 28 (2012) 4425–4433, https://doi.org/10.1021/la203097x.
[56] H. Yamada, C. Urata, Y. Aoyama, S. Osada, Y. Yamauchi, K. Kuroda, Preparation of colloidal mesoporous silica nanoparticles with different diameters and their unique degradation behavior in static aqueous systems, Chem. Mater. 24 (2012) 1462–1471, https://doi.org/10.1021/cm3001688.
[57] H.I. Meléndez-Ortiz, L.A. García-Cerda, Y. Olivares-Maldonado, G. Castruita, J. A. Mercado-Silva, Y.A. Perera-Mercado, Preparation of spherical MCM-41 molecular sieve at room temperature: influence of the synthesis conditions in the structural properties, Ceram. Int. 38 (2012) 6353–6358, https://doi.org/10.1016/j.ceramint.2012.05.007.
[58] L. Luo, Y. Liang, E.S. Erichsen, R. Anwander, Monodisperse mesoporous silica nanoparticles of distinct topology, J. Colloid Interface Sci. 495 (2017) 84–93, https://doi.org/10.1016/j.jcis.2017.01.107.
[59] S. Liu, et al., The influence of the alcohol concentration on the structural ordering of mesoporous silica: cosurfactant versus cosolvent, J. Phys. Chem. B 107 (2003) 10405–10411, https://doi.org/10.1021/jp034410w.
[60] S. Kachbouri, N. Mnasri, E. Elaloui, Y. Moussaoui, Tuning particle morphology of mesoporous silica nanoparticles for adsorption of dyes from aqueous solution, J. Saudi Chem. Soc. 22 (2018) 405–415, https://doi.org/10.1016/j.jscs.2017.08.005.
[61] K.S. Rao, K. El-Hami, T. Kodaki, K. Matsushige, K. Makino, A novel method for synthesis of silica nanoparticles, J. Colloid Interface Sci. 289 (2005) 125–131, https://doi.org/10.1016/j.jcis.2005.02.019.
[62] L.M. Rossi, L. Shi, F.H. Quina, Z. Rosenzweig, Stöber synthesis of monodispersed luminescent silica nanoparticles for bioanalytical assays, Langmuir 21 (2005) 4277–4280, https://doi.org/10.1021/la0504098.
[63] H. Yamada, H. Ujiie, C. Urata, E. Yamamoto, Y. Yamauchi, K. Kuroda, A multifunctional role of trialkylbenzenes for the preparation of aqueous colloidal mesostructured/mesoporous silica nanoparticles with controlled pore size, particle diameter, and morphology, Nanoscale 7 (2015) 19557–19567, https://doi.org/10.1039/C5NR04465K.
[64] Á.A. Beltrán-Osuna, J.L. Gómez Ribelles, J.E. Perilla, Effects of commonly unreported physicochemical variables on the morphology of mesoporous silica nanoparticles type MCM-41, J. Nanoparticle Res. 19 (2017) 1–14, https://doi.org/10.1007/s11051-017-4077-2.
[65] T.W. Kim, P.W. Chung, V.S.Y. Lin, Facile synthesis of monodisperse spherical MCM-48 mesoporous silica nanoparticles with controlled particle size, Chem. Mater. 22 (2010) 5093–5104, https://doi.org/10.1021/cm1017344.
[66] T. Yokoi, T. Karouji, S. Ohta, J.N. Kondo, T. Tatsumi, Synthesis of mesoporous silica nanospheres promoted by basic amino acids and their catalytic application, Chem. Mater. 22 (2010) 3900–3908, https://doi.org/10.1021/cm9037846.
[67] W.Y. Sang, O.P. Ching, Tailoring MCM-41 mesoporous silica particles through modified sol-gel process for gas separation, Oct, in: AIP Conference Proceedings, American Institute of Physics Inc., 2017, https://doi.org/10.1063/1.5005480, 020147.
[68] T. Yokoi, et al., Mechanism of formation of uniform-sized silica nanospheres catalyzed by basic amino acids, Chem. Mater. 21 (2009) 3719–3729, https://doi.org/10.1021/cm900993b.
[69] K. Kuperkar, et al., Viscoelastic micellar water/CTAB/NaNO3 solutions: rheology, SANS and cryo-TEM analysis, J. Colloid Interface Sci. 323 (2008) 403–409, https://doi.org/10.1016/j.jcis.2008.04.040.
[70] V. Agarwal, M. Singh, G. McPherson, V. John, A. Bose, Microstructure evolution in aqueous solutions of cetyl trimethylammonium bromide (CTAB) and phenol derivatives, Colloids Surfaces A Physicochem. Eng. Asp. 281 (2006) 246–253, https://doi.org/10.1016/j.colsurfa.2006.02.047.
[71] R.M. Pallares, X. Su, S.H. Lim, N.T.K. Thanh, Fine-tuning of gold nanorod dimensions and plasmonic properties using the Hofmeister effects, J. Mater. Chem. C 4 (2016) 53–61, https://doi.org/10.1039/C5TC02426A.
[72] K. Möller, J. Kobler, T. Bein, Colloidal suspensions of nanometer-sized mesoporous silica, Adv. Funct. Mater. 17 (2007) 605–612, https://doi.org/10.1002/adfm.200600578.
[73] P.P. Ghimire, M. Jaroniec, Renaissance of Stöber method for synthesis of colloidal particles: new developments and opportunities, J. Colloid Interface Sci. 584 (2021) 838–865, https://doi.org/10.1016/j.jcis.2020.10.014.
[74] S. Fouilloux, O. Taché, O. Spalla, A. Thill, Nucleation of silica nanoparticles measured in situ during controlled supersaturation increase. Restructuring toward a monodisperse nonspherical shape, Langmuir 27 (2011) 12304–12311, https://doi.org/10.1021/la2013842.
[75] R. Kumar, H.T. Chen, J.L.V. Escoto, V.S.Y. Lin, M. Pruski, Template removal and thermal stability of organically functionalized mesoporous silica nanoparticles, Chem. Mater. 18 (2006) 4319–4327, https://doi.org/10.1021/cm060598v.
[76] A. Lodha, et al., Synthesis of mesoporous silica nanoparticles and drug loading of poorly water soluble drug cyclosporin A, J. Pharm. BioAllied Sci. 4 (2012) 92–94, https://doi.org/10.4103/0975-7406.94153.
[77] J. Kobler, K. Möller, T. Bein, Colloidal suspensions of functionalized mesoporous silica nanoparticles, ACS Nano 2 (2008) 791–799, https://doi.org/10.1021/nn700008s.
[78] W. Stöber, A. Fink, E. Bohn, Controlled growth of monodisperse silica spheres in the micron size range, J. Colloid Interface Sci. 26 (1968) 62–69, https://doi.org/10.1016/0021-9797(68)90272-5.
[79] K.W. Gallis, C.C. Landry, Synthesis of MCM-48 by a phase transformation process, Chem. Mater. 9 (1997) 2035–2038, https://doi.org/10.1021/cm970482m.
[80] W.H. Fu, Y. Guan, Y.M. Wang, M.Y. He, A facile synthesis of monodispersed mesoporous silica nanospheres with Pm3n structure, Microporous Mesoporous Mater. 220 (2016) 168–174, https://doi.org/10.1016/j.micromeso.2015.09.004.
[81] B.N. Khlebtsov, V.A. Khanadeev, N.G. Khlebtsov, Determination of the size, concentration, and refractive index of silica nanoparticles from turbidity Sp[1] S. M. Mousavi Elyerdi, M. N. Sarvi, and A. J. O'Connor, "synthesis of ultra small nanoparticles (< 50 nm) of mesoporous MCM-48 for bio-adsorption,", Langmuir 24 (2008) 8964–8970, https://doi.org/10.1021/la8010053.
[82] Y.S. Lin, C.L. Haynes, Impacts of mesoporous silica nanoparticle size, pore ordering, and pore integrity on hemolytic activity, J. Am. Chem. Soc. 132 (2010) 4834–4842, https://doi.org/10.1021/ja910846q.
[83] S. Lechevallier, et al., Luminescence properties of mesoporous silica nanoparticles encapsulating different europium complexes: application for biolabelling, J. Nanomater. 2013 (2013) 11, https://doi.org/10.1155/2013/918369.
[84] Q. He, et al., The effect of PEGylation of mesoporous silica nanoparticles on nonspecific binding of serum proteins and cellular responses, Biomaterials 31 (2010) 1085–1092, https://doi.org/10.1016/j.biomaterials.2009.10.046.
[85] M. Varache, I. Bezverkhyy, F. Bouyer, R. Chassagnon, F. Baras, F. Bouyer, Improving structural stability of water-dispersed MCM-41 silica nanoparticles through post-synthesis pH aging process, J. Nanoparticle Res. 17 (2015) 356, https://doi.org/10.1007/s11051-015-3147-6.
[86] B. Moongraksathum, Y.W. Chen, Synthesis and size control of uniform, spherically shaped hexagonal mesoporous silica, J. Porous Mater. 26 (2019) 51–58, https://doi.org/10.1007/s10934-018-0609-0.
[87] D.M. Oliveira, A.S. Andrada, Synthesis of ordered mesoporous silica MCM-41 with controlled morphology for potential application in controlled drug delivery systems, Cerâmica 65 (2019) 170–179, https://doi.org/10.1590/0366-69132019653742509.
[88] M. Lindén, S.A. Schunk, F. Schüth, In situ X-ray diffraction study of the initial stages of formation of MCM-41 in a tubular reactor, Angew. Chem. Int. Ed. 37

(1998) 821–823, https://doi.org/10.1002/(SICI)1521-3773(19980403)37:6<821::AID-ANIE821>3.0.CO;2-I.
[89] N.T.K. Thanh, N. Maclean, S. Mahiddine, Mechanisms of nucleation and growth of nanoparticles in solution, Chem. Rev. 114 (2014) 7610–7630, https://doi.org/10.1021/cr400544s.
[90] M. Barczak, Template removal from mesoporous silicas using different methods as a tool for adjusting their properties, New J. Chem. 42 (2018) 4182–4191, https://doi.org/10.1039/c7nj04642a.